Aptian-Albian clumped isotopes from northwest China: Cool temperatures, variable atmospheric pCO$_2$ and regional shifts in hydrologic cycle

Dustin T. Harper[1], Marina B. Suarez[1,2], Jessica Uglesich[2], Hailu You[3,4,5], Daqing Li[6], Peter Dodson[7]

[1] Department of Geology, The University of Kansas, Lawrence, KS, U.S.A.
[2] Department of Geological Sciences, University of Texas, San Antonio, TX, U.S.A.
[3] Key Laboratory of Vertebrate Evolution and Human Origins, Institute of Vertebrate Paleontology and Paleoanthropology, Chinese Academy of Sciences, Beijing, P.R.C.
[4] Chinese Academy of Science Center for Excellence in Life and Paleoenvironment, Beijing, P.R.C.
[5] College of Earth and Planetary Sciences, University of Chinese Academy of Sciences, Beijing, P.R.C.
[6] Institute of Vertebrate Paleontology and College of Life Science and Technology, Gansu Agricultural University, Lanzhou, P.R.C.
[7] Department of Biomedical Sciences, The University of Pennsylvania, Philadelphia, U.S.A.

Correspondence to: Dustin T. Harper (dtharper@ku.edu)

Abstract. The Early Cretaceous is characterized by warm background temperatures (i.e., greenhouse climate) and carbon cycle perturbations that are often marked by Ocean Anoxic Events (OAEs) and associated shifts in the hydrologic cycle. Higher-resolution records of terrestrial and marine δ^{13}C and δ^{18}O (both carbonates and organics) suggest climate shifts during the Aptian-Albian, including a warm period associated with OAE 1a in the early Aptian and subsequent "cold snap" near the Aptian-Albian boundary prior to the Kilian and OAE 1b. Understanding the continental system is an important factor in determining the triggers and feedbacks to these events. Here, we present new paleosol carbonate stable isotopic (δ^{13}C, δ^{18}O and Δ_{47}) and CALMAG weathering parameter results from the Xiagou and Zhonggou Formations (part of the Xinminpu Group in the Yujingzi Basin of NW China) spanning the Aptian-Albian. Published mean annual air temperature (MAAT) records of the Barremian-Albian from Asia are relatively cool with respect to the Early Cretaceous. However, these records are largely based on coupled δ^{18}O measurements of dinosaur apatite phosphate (δ^{18}O$_p$) and carbonate (δ^{18}O$_{carb}$), and therefore rely on estimates of meteoric water δ^{18}O (δ^{18}O$_{mw}$) from δ^{18}O$_p$. Significant shifts in the hydrologic cycle likely influenced δ^{18}O$_{mw}$ in the region, complicating these MAAT estimates. Thus, temperature records independent of δ^{18}O$_{mw}$ (e.g., clumped isotopes or Δ_{47}) are desirable, and required to confirm temperatures estimated with δ^{18}O$_p$ and δ^{18}O$_c$, and to reliably determine regional shifts in δ^{18}O$_{mw}$. Primary carbonate material was identified using traditional petrography, cathodoluminescence inspection, and δ^{13}C and δ^{18}O subsampling. Our preliminary Δ_{47}-based temperature reconstructions (record mean of 14.9 ºC), which we interpret as likely being representative of MAAT, match prior estimates from similar paleolatitudes of Asian MAAT (average ~15 ºC) across the Aptian-Albian. This, supported by our estimated mean atmospheric paleo-pCO$_2$ concentration of 396 ppmv, indicates relatively cooler mid-latitude terrestrial climate. Additionally,

our coupled $\delta^{18}O$ and Δ_{47} records suggest shifts in the regional hydrologic cycle (i.e., ΔMAP and $\Delta\delta^{18}O_{mw}$) that may track Aptian-Albian climate perturbations (i.e., a drying of Asian continental climate associated with the cool interval).

1 Introduction

Early Cretaceous climate is characterized by a warm background greenhouse climate state and perturbations to climate and the carbon cycle associated with shifts in global $\delta^{13}C$, including Cretaceous Ocean Anoxic Events (OAEs; Föllmi, 2012; Hay, 2016; Jenkyns, 2018). Such climate aberrations can provide insight into the sensitivities and coupling of the carbon cycle, climate and the hydrologic cycle through quantitative reconstruction of past physical and environmental conditions (e.g., atmospheric paleo-pCO$_2$, temperature and precipitation). Indeed, much work has been done generating geochemical proxy-based observations and simulations of past global warming events which serve as useful analogues of future warming (e.g., Zachos et al., 2008; Hönisch et al., 2012; Hay, 2016). Similarly, both long-term and abrupt cooling intervals in the past can supply proxy-based observations of negative climate feedbacks associated with carbon sequestration and global cooling.

Multiple climate events (including OAEs) have been identified during the late Early Cretaceous (Jenkyns, 2018; Vickers et al., 2019) oftentimes referred to as the mid-Cretaceous (i.e., here, our records span the Aptian-Albian; 125 to 100.5 Ma). While limited, available temperature records (e.g., Jenkyns, 2018) and high latitude sedimentological evidence (Vickers et al., 2019) suggest a relatively cool interval (following warmth during OAE 1a) associated with a global carbon isotope maximum (i.e., "C10"; Menegatti et al., 1998; Bralower et al., 1999; Mutterlose et al., 2009) at the Aptian-Albian boundary prior to OAE 1b (Bottini et al., 2015). Estimates of Aptian-Albian atmospheric paleo-pCO$_2$, while highly uncertain, tend to suggest low (less than 1000 to 1500 ppmv background greenhouse climate conditions; Franks et al., 2014) concentrations at the Aptian-Albian consistent with a cooler climate (Ekart et al., 1999; Wallmann, 2001; Fletcher et al., 2005; Aucour et al., 2008; Passalia, 2009; Haworth et al., 2010; Du et al., 2018). This C10 interval has been identified on land using stable isotopes in terrestrial paleosol carbonates and organic carbon from the continental interiors of North America (Ludvigson et al., 2010; Suarez et al., 2014) and Asia (Suarez et al., 2018). For Asia, Aptian-Albian terrestrial temperature estimates have been generated using oxygen isotopes in dinosaur tooth enamel (Amiot et al., 2011) and suggest a relatively cool interval (e.g., ~10 ± 4 ºC mean annual air temperature, MAAT; ~42 ºN paleolatitude) consistent with marine paleotemperatures (Mutterlose et al., 2009; Bottini et al., 2015) and elevated global $\delta^{13}C$ (Menegatti et al., 1998; Bralower et al., 1999). However, MAAT estimates from $\delta^{18}O$ of dinosaur tooth enamel phosphate ($\delta^{18}O_p$) hinge on the relationship between mean annual temperature, latitude and the $\delta^{18}O$ of meteoric water or $\delta^{18}O_{mw}$ (Amiot et al., 2004). $\delta^{18}O_{mw}$ is influenced by other parameters in addition to temperature and latitude, and is further complicated as the intensity of poleward moisture transport is altered by greenhouse climate conditions. Therefore, confirming these temperatures with a secondary geochemical proxy is warranted.

Hydrologic cycle models and observations of past warm intervals (e.g., early Cenozoic and greenhouse Cretaceous) indicate an "intensification" of the hydrologic cycle due to enhanced poleward moisture transport associated with global warming

70 (White et al., 2001; Poulsen et al., 2007; Suarez et al., 2011a; Hasegawa et al., 2012; e.g., Carmichael et al., 2015). Likewise, as temperatures cool during Cretaceous climate recovery or during long-term transitions driven by changes in global tectonics and paleogeography, the hydrologic cycle tends to respond with regionally dependent shifts in mean annual precipitation (MAP). For example, Hasegawa et al. (2012) observed hydrologic cycle responses track greenhouse gas (GHG) forcing in Asia during the mid-Cretaceous. For the Aptian-Albian, models and observations suggest changes in continental

75 interior precipitation during the global "cold snap" (e.g., Mutterlose et al., 2009) and the potential for variable Asian aridity associated with warm/cool cycles (Poulsen et al., 2007; Zhou et al., 2008; Hasegawa et al., 2010; Hasegawa et al., 2012; Föllmi, 2012; Tabor et al., 2016), which may hamper $\delta^{18}O_P$-based temperature reconstructions for the Aptian-Albian that fail to quantify $\delta^{18}O_{mw}$ independently of $\delta^{18}O_P$. To address this deficiency, here we provide new multi-proxy records from the Yujingzi Basin of NW China spanning the Aptian-Albian using $\delta^{13}C$, $\delta^{18}O$ and Δ_{47} (i.e., clumped isotopes) of terrestrial

80 paleosol carbonates. Additionally, MAP is quantified using chemical weathering ratios, specifically CALMAG (Nordt and Driese, 2010). We combine our new records with organic stable carbon isotope chemostratigraphic records for the site (Suarez et al., 2018) to provide age control to quantitatively interpret shifts in regional temperature, $\delta^{18}O_{mw}$, MAP, and global atmospheric paleo-pCO$_2$ associated with the Aptian-Albian. These proxy interpretations are compared to models and records of Cretaceous Asian climate and the global exogenic carbon cycle (i.e., atmospheric paleo-pCO$_2$) to provide new

85 constraints on Aptian-Albian climate, carbon and hydrologic cycles.

2 Materials and methods

2.1 Sampling and analyses

The Xiagou and Zhonggou Formations, part of the Xinminpu Group in the Yujingzi Basin of Northwest China (Gansu Province), were sampled in 2011 with the goal of placing the Early Cretaceous paleobiology and geology of this region in a

90 global climate and carbon isotope chemostratigraphic framework (e.g., Suarez et al., 2018). The Xinminpu Group, approximately Early Cretaceous in northwest China, is composed of four formations (ordered stratigraphically bottom to top): Chijinqiao Formation, Chijinpu Formation, Xiagou Formation, and Zhonggou Formation. Outside of the Yujingzi Basin, Xinminpu group strata produce Aptian radiometric dates of 123.0 ± 2.6 to 133.7 ± 1.8 Ma (Li et al., 2013; Kuang et al., 2013). Additionally, a recent study (Zheng et al., 2021) establishes regional ages through bio- and chronostratigraphy.

95 They review available age controls for the lower Cretaceous in northwest China and place the organic carbon isotope records of Suarez et al. (2018) (i.e., our study sections) within the chronostratigraphic framework of the region. Zheng et al. (2021) provide additional evidence that our study section spans the "C10" interval at the Aptian-Albian boundary. Outcrop sections (Fig. 1) are regionally exposed in the Yujingzi basin at a fossil-rich site informally known as the White Pagoda Site,

100 produced by accommodation of strike-slip motion from Lhasa Block convergence with Asia (Chen and Yang, 1996; Vincent and Allen, 1999).

Outcrop sections for White Pagoda were numbered and split into three facies by Suarez et al. (2018): 1) the lowermost facies consisting of sections 1, 2, 2A, dominated by sandstones, 2) an overlying facies of alternating gray and variegated mudstones

105 and muddy sandstones consisting of sections 3, 3A-H, and 6, and 3) coarse-grained poorly sorted arkosic sandstones and sandy mudstones (Section 4). Here, we utilize sample material from sections (in stratigraphic order) 3, 3A-H, 6, and 4 (see Supplementary Material Fig. S1 for lithostratigraphic details). Suarez et al. (2018) observed carbonate nodules, root-traces, charophytes, turtle remains, ostracodes and gastropods within the middle facies (Sections 3, 3A-H, and 6), with root-traces and nodules extending into the uppermost facies (Section 4). Section 4 had a higher degree of color-mottling, blocky ped-

110 structures and burrows compared to the underlying facies. Facies interpretations for sections sampled for this study indicate fluvio-lacustrine and palustrine environments (i.e., Suarez et al., 2018). For example, sections 3, 3A-H, 6, and 4 exhibit evidence of subaerial exposure (soils indicated by horizonation, slickensides, root traces and carbonate nodule formation), fluvial deposition (lenticular sands fining up with erosive bases), and lacustrine environments (turtle remains, charophytes, ostracodes, thin limestones, and organic-rich mudstones) (Suarez et al., 2018; Fig. 1). For the sections of interest, the

115 presence of cracking, slickensides (mukkara structures) and expansive clays suggests wet/dry periods typical of vertisols (Fig. 1).

The organic stable carbon isotope record at White Pagoda was used as a guide to sample carbonate nodules for analysis. Specifically, samples were selected to span deposition before during and after carbon isotope excursions of interest, namely

120 the C10 excursion. Nodules for analysis were sampled from well below channel sands and surface paleosol horizons in outcrop (i.e., sampled from paleosol B horizons; Tabor and Myers, 2015) to help avoid potential surficial biases on carbonate (e.g., radiative heating in soil depths <50 cm; Burgener et al., 2019). Paleosols from which nodules are sampled are fine grained throughout the section which suggests suitability for clumped isotope-based MAAT interpretation (e.g., Kelson et al., 2020).

125

Thin sections were cut from hand samples for petrographic analysis and cathodoluminescence (CL) imaging to aid in the identification and isolation of primary carbonate nodule material. Briefly, thin sections were inspected for environmental indicators and microfabrics, and photographed under plane-polarized and cross-polarized light (PPL and XPL, respectively) using an Olympus BX43P petrographic microscope with a SC50 Olympus camera. Thin sections were then CL imaged using

130 a Relion Industries Reliotron III cold-cathode chamber, with operating conditions consisting of a rarified helium atmosphere at 50 milliTorr, accelerating voltage of 10 kV, and beam current of 0.5 mA (i.e., conditions for high luminescence sensitivity). Macroscale imaging through the 50 mm top window of the chamber was carried out using a 16 Mpx Canon EOS SL1 DSLR camera with a macro lens suspended over the CL chamber. Microphotography of CL images was taken with an

Olympus BX41 compound microscope and DP73 17megapixel Olympus camera at the Kansas Geologic Survey. CL
imaging was used to detect any heterogeneities in cation substitution which may indicate alteration, as Mn^{2+} tends to
substitute for Ca^{2+} in reducing conditions generating bright orange luminescence (Habermann et al., 2000; Cazenave et al.,
2003). While luminescence in biogenic carbonates (e.g., mollusk shells) indicate diagenetic alteration from the original
carbonate, high luminescence does not always indicate degree of diagenesis in soil and palustrine carbonates which likely
form in conditions that are alternately saturated and reducing and unsaturated and oxidative as water tables fluctuate.
(Ludvigson et al. 2010; Mintz et al., 2011).

Once located in thin section using petrography and CL, primary nodule carbonate was mapped onto the corresponding thin-
section billet, and sampled using a dental drill. In some samples, suspect non-primary carbonate material (e.g., spar) was also
sampled for isotopic comparison, but excluded from primary carbonate isotopic averages reported here. Depending on the
number of nodules and lithologic complexity of a hand sample, approximately 8 to 14 ~50 μg samples were drilled for
traditional stable isotopes (i.e., $\delta^{13}C$ and $\delta^{18}O$) in each hand sample. Stable isotope samples were heated to 200 ºC in a
vacuum for 1 hour prior to analysis via ThermoFinnigan MAT 253 gas source isotope ratio mass spectrometer (IR-MS)
coupled to a Kiel IV carbonate device at the University of Kansas (KU) Keck-NSF Paleoenvironmental and Environmental
Stable Isotope Laboratory (KPESIL). Standard reproducibility indicates analytical precision (1σ) of 0.03‰ and 0.05‰ for
$\delta^{13}C$ and $\delta^{18}O$, respectively.

Following $\delta^{13}C$ and $\delta^{18}O$ analysis of dental-drilled carbonate powder, larger samples (~6 mg of material for each analysis; n
= 4 per sample with the exception of one sample with n = 3), were drilled for clumped isotope (Δ_{47}) analysis from areas of
primary nodule carbonate exhibiting uniform $\delta^{13}C$ and $\delta^{18}O$, and CL. Our pedogenic carbonate nodules were cm to multi-cm
in scale, providing ample carbonate material for sampling. Clumped isotopes were measured at the University of Colorado
Boulder (UCB) Earth Systems Stable Isotope Laboratory (CUBES-SIL) on a custom automated vacuum line sample
introduction system, in which samples are digested at 90 ºC in a common phosphoric acid bath. This system removes
isobaric contamination by entraining the CO_2 sample in helium and passing it through a ~1.5 m long stainless steel column
hand packed with Poropak for 45 minutes at −20 °C. CO_2 is transferred to the sample side bellow of a ThermoFinnigan dual
inlet MAT 253+. Values are reported relative to the carbon dioxide equilibration scale (Dennis et al., 2011), using gases with
a range of bulk δ^{47} values and equilibrated at 1000 °C and 25 °C to convert in-house values to the CDES scale. IUPAC
parameters for ^{17}O corrections (Brand et al., 2010) were used in the initial steps of data reduction, following
recommendations of (Daëron et al., 2016) and (Schauer et al., 2016). We then applied an acid correction factor (0.088‰)
appropriate for use with values calculated using IUPAC parameters (Petersen et al., 2019). In addition to the heated and
equilibrated gas reference frame, international carbonate standards (i.e., ETH1, ETH2, ETH3, ETH4, IAEA-C1, IAEA-C2,
Merck and NBS19) were utilized to further correct Δ_{47} values (see Supplementary Table S1 for acquired standard values).
Potentially contaminated data was culled (e.g., sample analyses which exhibit Δ_{48} excess that tracks variability in Δ_{47}; see

Supplementary Material). Replicate analyses tended to be highly consistent (see Supplementary Material; Table S2 and S3 for raw data).

X-Ray Fluorescence (XRF) measurements were carried out on samples from horizons that appear to be well-developed paleosols, specifically horizons interpreted as B-horizons. Analysis was completed with a Rigaku Primus II WD-XRF spectrometer at the University of Texas at San Antonio. Raw X-ray intensities were calibrated by the analysis of eight USGS certified elemental standards (BIR-1a, COQ-1, DNC-1a, GSP-2, RGM-2, SBC-1, STM-2, W-2a), with an RSD value of 0.036%. Weight percentages were converted into molar weights before application of a chemical index, following Sheldon and Tabor (2009). Al_2O_3, CaO, and MgO are the oxides used for calculation of the CALMAG (Nordt and Driese, 2010) chemical weathering index (see following section for parameter calculation and proxy details).

2.2 Quantitative proxies

Clumped isotopes (i.e., Δ_{47}) have been successfully utilized to estimate temperature in carbonates, leveraging the thermodynamically controlled abundance of isotopically heavy ^{13}C and ^{18}O bonded isotopes (Ghosh et al., 2006; Schauble et al., 2006) relative to a stochastic abundance of such "clumps". This approach has an advantage over $\delta^{18}O$-based temperature estimates, as other controlling variables (e.g., $\delta^{18}O_{mw}$) need not be estimated. Δ_{47} values are translated into calcification temperature following the calibration of Petersen et al. (2019) and we define our temperature uncertainty as 2σ, or twice the mean propagated external precision (1σ) of each Δ_{47} analysis, as this likely captures compounded uncertainties in our temperature estimates (Fernandez et al., 2017; Bernasconi et al., 2021). We also include 2SE uncertainty for Δ_{47} (Fig. 5 and Supplementary Material (Table S3). Additional temperature calibration approaches (i.e., Ghosh et al., 2006; Bonifacie et al., 2017) and calculation details (i.e., R code for data analysis) are available in the Supplementary Material. However, for this study, in subsequent calculations and figures, we opt for Petersen et al. (2019) Δ_{47} values and calibration temperatures calculated using the following relationship:

$$\Delta_{47} = (0.0383 \pm 1.7^{-6}) \times (10^6 / T^2) + (0.258 \pm 1.7^{-5}) \qquad (1)$$

Groundwater $\delta^{18}O$ is derived from the oxygen isotopic composition of precipitation which is ultimately controlled by factors such as temperature, amount, continentality and seasonality. It can be further modified by processes such as evaporation in paleoenvironments which experience wet/dry cycles. $\delta^{18}O$ of groundwater ($\delta^{18}O_w$) can be determined for pedogenic carbonate calcification once temperature is known and $\delta^{18}O_{carb}$ is measured following Friedman and O'Neil (1977):

$$\delta^{18}O_w \text{ (SMOW)} = (\delta^{18}O_{carb} \text{ (SMOW)} + 10^3) / (e^{(18030 / T - 32.42) / 1000}) - 10^3 \qquad (2)$$

To estimate mean regional precipitation for the study interval and determine shorter-term precipitation variability in our record, we use the bulk geochemical compositional proxy CALMAG (Nordt and Driese, 2010), which utilizes the gains and

losses of elemental oxide abundances as a result of weathering in vertisols. The concentration of aluminum oxide, calcium oxide and magnesium oxide are estimated using XRF and the CALMAG parameter is determined:

$$CALMAG = (Al_2O_3) / (Al_2O_3 + CaO + MgO) \times 10^2 \quad (3)$$

Mean annual precipitation (MAP) is then determined from the CALMAG parameter based on the Nordt and Driese (2010) calibration:

$$MAP = 22.69 \times (CALMAG) - 435.8 \quad (4)$$

Paleosols have been widely utilized as archives to determine the past concentration of atmospheric pCO_2 (Cerling, 1991; Ekart et al., 1999). While requiring a number of assumptions, soil carbonate nodule $\delta^{13}C$, when used in tandem with estimates from other proxies (e.g., MAP from CALMAG and respired soil $\delta^{13}C_{CO2}$ from $\delta^{13}C_{org}$), provide many of the most robust estimates of Cretaceous atmospheric pCO_2 outside of a stomatal approach (Franks et al., 2014), especially because paleosol carbonate nodules are abundant in the rock record. The soil carbonate paleobarometer uses a diffusion model in which atmospheric pCO_2 ($\delta^{13}C_a$) and respired CO_2 from soils ($\delta^{13}C_r$) are the dominant controls on soil CO_2 ($\delta^{13}C_s$) following the mixing model of Cerling (1991) in terms of $\delta^{13}C$ (Ekart et al., 1999). The relative isotopic influence of atmospheric versus respired soil CO_2 on soil CO_2 (i.e., the source CO_2 for calcite) will therefore be controlled by the concentration of CO_2 in the atmosphere, if the concentration of the soil-derived component of total gas at depth, S(z), is accounted for following Ekart et al. (1999):

$$pCO_2 = S(z) \times ((\delta^{13}C_s - 1.0044 \times \delta^{13}C_r - 4.4 / (\delta^{13}C_a - \delta^{13}C_s)) \quad (5)$$

$\delta^{13}C_s$ can be determined from $\delta^{13}C_{carb}$, assuming temperature-dependent fractionation (here we use Δ_{47}-based temperature) between gaseous soil CO_2 and carbonate (Romanek et al., 1992). Suarez et al. (2018) correlated sections in this study to bulk carbonate surface marine sections using $\delta^{13}C$ chemostratigraphy. We estimate atmospheric $\delta^{13}C$ (i.e., $\delta^{13}C_a$) from a marine section correlated chemostratigraphically with the White Pagoda Site (i.e., Peregrina Canyon, Mexico of Bralower et al. (1999) correlated to White Pagoda by Suarez et al. (2018)), applying a $\delta^{13}C_{DIC}$ (i.e., $\delta^{13}C$ of marine dissolved inorganic carbon, DIC) to $\delta^{13}C_a$ fractionation of -8.23‰ consistent with "greenhouse climate" carbon cycle simulations (i.e., Zeebe, 2012), and assuming bulk carbonate $\delta^{13}C$ for the Peregrina Canyon section is representative of global surface DIC $\delta^{13}C$. This results in $\delta^{13}C_a$ values ranging from -5.38 to -4.18 in samples used to compute pCO_2. For $\delta^{13}C_r$, we apply the bulk sedimentary organic carbon $\delta^{13}C$ values of Suarez et al. (2018).

In addition to estimates of $\delta^{13}C$ for the three carbon reservoirs outlined above, the term S(z), or the depth-dependent contribution of soil-respired CO_2, must be determined to compute atmospheric paleo-pCO_2. While this term is a significant source of uncertainty due in part to a large range of potential past environmental conditions, Cotton and Sheldon (2012) hypothesized a relationship between summer minimum S(z) and MAP using observations of modern soils:

$$S(z) = 5.67 \times MAP - 269.9 \quad (6)$$

Here, we apply their relationship to compute S(z) from our CALMAG-based MAP estimates. It is important to note that the relationship defined by Cotton and Sheldon (2012) uses a dataset which does not include humid climate soils or vertisols, and it is therefore cautiously applied and discussed in terms of paleoenvironmental influence on our paleo-pCO$_2$ estimates (i.e., we evaluate our atmospheric pCO$_2$ record against a large range in S(z)).

3 Results

3.1 Petrography

Based on carbonate petrography we recognize two distinct microfacies in our samples and split samples into two groups (microfacies (i) and (ii)) to evaluate the origin of stable isotope values (primary vs. secondary; depositional environment) (Fig. 2; Table 1). Microfacies (i) is characterized by distinct nodules which originated from primarily clayey horizons, consisting of dense micrite with abundant root traces and fractures filled with sparry calcite and microspar calcite (Fig. 2). Fracturing is less pervasive and micritic nodules include less clay minerals in microfacies (i). Nodule micrite is dull to brightly luminescent under CL and secondary spar filled fractures and voids tend to be non-luminescent or dull. The clay matrix displays birefringent microfabric and contains subangular to subrounded clasts of calcic and siliciclastic grains (mainly quartz and feldspars as well as fragments of other nodules) (Fig. 3). Microfacies (i) includes samples 3-021, 3A-097, 4-038, and 3H-014.

Samples in microfacies (ii) (observed in samples 3B-021, 3E-001, 6-003, and 6-042), tend to be coalesced nodules or beds comprised almost entirely of clay-rich microcrystalline calcite in which discreet nodules are less evident (e.g., samples 3E-001 and 6-042; Fig. 3). Microfacies (ii) shows dull yellow to orange luminescence of the micrite with brightly luminescent spar-filled fracture voids. The microfacies displays a higher degree of CL heterogeneity (i.e., patchiness). For example, Mn staining tends to luminesce to a greater degree than surrounding non-Mn-stained micrite (Fig. 3). The second microfacies is characterized by clay-rich (i.e., common to frequent in abundance) micritic limestone with abundant fracturing and brecciation, including circum-granular fractures (i.e., sample 6-042; Fig. 3). These are filled with microspar and spar (Fig. 2). Color mottling and Mn-staining are observed, perhaps related to microbial activity (i.e., thrombolites and/or pisoids; Fig. 2b). Sample 3F-019 appears to be a mixture of the two microfacies, with dense, brightly luminescent (i.e., CL) micritic nodules in dominantly clay matrix, mottled coloring in thin section, rhizoliths, circum-granular fractures and Mn-staining (Fig. 2 panel c). Nodules appear slightly coalesced in this sample (i.e., unlike microfacies (i)), whilst individual nodule shape is somewhat maintained (i.e., unlike microfacies (ii)). CL displayed by White Pagoda samples is consistent with previous descriptions of vertic soil carbonate in which dull to lightly luminescent primary nodule carbonate is differentiated with either non-luminescing (early) or brightly luminescing (late) secondary material (Driese and Mora, 1993). In addition, variation in luminescence of soil carbonates from modern vertisols (Mintz et al., 2011) emphasizes that soil carbonates can often be precipitated and stabilized in varying Eh environments that can affect the luminescence of primary carbonate.

3.2 Traditional stable and clumped isotopes

Stable isotopes of drill spot samples show a high degree of intrasample homogeneity (Fig. 4). Measurements between University of Kansas and University of Colorado, Boulder are largely consistent with comparable precision (Tables 1 and 2; Fig. 4). $\delta^{13}C$ values range from −8‰ to −3‰ and $\delta^{18}O$ ranges from −12‰ to −6‰ for carbonates measured in this study. Sample 3B-021 displays the most heavy-isotope enriched $\delta^{13}C$ and $\delta^{18}O$ values, with $\delta^{13}C$ more than 2‰ and $\delta^{18}O$ more than 1‰ greater than all other samples (Fig. 4), despite the relative isotopic low in the $\delta^{13}C_{org}$ curve which results in a large $\Delta^{13}C$ for that sample (Table 1). Carbonate samples tend to be isotopically homogenous ($2\sigma \leq 0.6$‰ for all sample $\delta^{13}C$ and $\delta^{18}O$, with only 2 samples with $2\sigma > 0.3$‰; Table 1) following Cotton and Sheldon (2012), who proposed a requirement of $2\sigma < 0.5$‰ for $\delta^{13}C$ and $\delta^{18}O$ for all samples applied to paleo-pCO$_2$ reconstructions. We discern no relationship between $\delta^{13}C$ and $\delta^{18}O$ of carbonates, nor grouping of microfacies by stable isotopic composition (e.g., Fig. 4; Table 1).

Clumped isotope (Δ_{47}) mean sample values range from 0.707 to 0.732‰ (Table 2) which, following the Petersen et al. (2019) calibration, translates to temperatures ranging from ~10 to 20 ºC, with an average temperature of 14.9 ºC for the entire record. Transient cooling of ~2 to 4 ºC (i.e., down to 11.1 ºC) is observed in the C10 carbon isotope interval, with the warmest temperature occurring immediately following the C10 interval (i.e., warms to 18.8 ºC; Fig. 5). Temperature variation tends to be smaller in magnitude than 2σ temperature uncertainty.

3.3 CALMAG

CALMAG values for all measured samples range from a low of 2 to a high of 70. Lowest values are either samples that were not identified as B-horizons or likely immature soils which yield values inapplicable to range in calibration (CALMAG less than ~35; Supplementary Table S4). If only B-horizon samples applicable to the range in the Nordt and Driese (2010) calibration are considered, maximum variability in CALMAG is ± 12 (Table 3; Supplementary Table S4). This translates to MAP variability of ± 270 mm/yr over the interval, with mean MAP of 641 mm/yr (i.e., mean CALMAG of 47.5) for paleosols in which clumped isotopes were also measured (Table 3; Fig. 5).

4 Discussion

4.1 Carbonate nodule $\delta^{13}C$ and $\delta^{18}O$

Light stable isotopes ($\delta^{13}C$ and $\delta^{18}O$) of carbonate material measured at KU and CUB are consistent (Tables 1 and 2; Fig. 4) indicating primary carbonate was successfully sampled from nodules for clumped isotope analyses (i.e., primary carbonate isotopic composition characterized by drill spot measurements at KU match values from CUB clumped measurements). $\delta^{13}C$ in carbonate nodules is controlled by soil water DIC which, through time, is ultimately controlled by variation in the other exogenic carbon reservoirs. Carbonate $\delta^{18}O$ is reflective of regional meteoric water and temperature. Though much coarser

resolution, our carbonate $\delta^{13}C$ largely follows $\delta^{13}C_{org}$ which has been tied to global variations in the carbon cycle (Ando et al., 2002; Heimhoffer et al., 2003; Ludvigson et al., 2010; Ludvigson et al., 2015; Suarez et al., 2018), suggesting both carbonate and organic records at the site track global variability in the carbon cycle originally described in Menegatti et al.

340   (1998) and Bralower et al. (1999) (Fig. 5) (e.g., $\delta^{13}C_{carb}$ is highest in the C10 interval). We observe no clear grouping of carbonate stable isotopes by microfacies and all samples contain pedogenic features. This suggests $\delta^{13}C_{carb}$ tracks global variations in the carbon cycle, and $\delta^{18}O_{carb}$ values are reflecting $\delta^{18}O$ of regional precipitation once temperature is considered.

4.2 Interpreting paleoenvironmental biases in Δ_{47}-based temperatures

345   Macroscopic features described in Suarez et al. (2018) along with traditional carbonate petrography suggest a paleoenvironment which experienced wet/dry cycles. These features include redoximorphic color mottling, gilgai structures and mukkara cracks (Fig. 1), fracturing pervasive to varying degrees in carbonate nodules, microspar and spar recrystallization present in voids/fractures, Mn staining and root traces (Fig. 1, 2 and 3). Microscopic features are consistent with facies interpretations of Suarez et al. (2018) which suggest fluvio-palustrine paleoenvironment. Rhizoliths (i.e.,

350   calcified root structures) in nearly all nodule samples (e.g., Fig. 1 and 2) indicate that vegetation was present and the carbonate nodules are indeed soil-formed in subhumid to semiarid conditions (Zhou and Chafetz, 2009). Indeed, mean MAP derived from our CALMAG proxy record suggests 712 mm/yr (respective minimum and maximum MAP of 476 and 984 mm/yr for the interval; Fig. 5) and Δ_{47}-based temperatures range from 11.4 °C (+7.5 / −7.0 °C; 2σ) to 18.8 °C (+9.2 / −8.4 °C; 2σ), consistent with the subhumid to semiarid environments in which soil carbonates commonly form (Birkeland et al., 1999;

355   Zhou and Chafetz, 2009; Breecker et al., 2009).

Understanding the timing of carbonate formation in soils is important for interpretation of $\delta^{13}C$, $\delta^{18}O$ and Δ_{47}. The solubility of calcite is the primary controlling factor on carbonate formation, and it is significantly affected by soil CO_2 concentration. Because CO_2 concentration is lower in warmer conditions, and drier conditions result in greater concentration of ions, calcite

360   precipitation tends to occur during warm, dry conditions. Numerous early studies have suggested warm season bias in soil carbonate formation and thus the Δ_{47}-derived temperatures (Breecker et al., 2009; Passey et al., 2010). Recent work of Kelson et al. (2020) suggests this may not always be the case for a number of reasons. The presence of vegetation (suggested by abundant root traces) may shade the soil surface from solar radiation. However, Burgener et al. (2019) and Kelson et al. (2020) found that this effect is rare, and samples for this study were collected from paleosol horizons deep enough (i.e., > 50

365   cm) to be buffered against the effects of radiative heating (i.e., Burgener et al., 2019). Seasonality of precipitation, evaporation, and evapotranspiration likely affects the degree to which a warm season temperature bias may occur. In a study of modern soils in North America, Gallagher and Sheldon (2016) suggested that only continental climate with rainy seasons in the spring had summer temperature biases. Suarez et al. (2011b) suggested that lower than expected temperatures of Mio-

Pliocene soil carbonates from the Chinese Loess Plateau may be the result of a monsoon climate in which the rainy seasons occur during the warmest part of the season and conditions for calcite precipitation occurs prior to or after the warm season.

375

These studies suggest that carbonate nodule clumped isotope-based temperatures revealed from the Xinminpu Group likely represent lower temperatures than mean warm season. In addition, mean clumped isotope-based temperature over the study interval (14.9 ºC) matches Aptian-Albian MAATs derived from phosphate $\delta^{18}O$ in dinosaur teeth from similar paleolatitudes in Asia (i.e., 15 ºC for Xinminpu group; Amiot et al., 2011). However, our mid-latitude continental interior temperatures reflect the temperature of calcite precipitation and may be biased towards the time of year during which a region experiences its first month without water storage, which varies by regional climate (Gallagher and Sheldon, 2016). Given our paleoenvironmental interpretation of wet-dry seasonality which resulted in vertisol formation at our study location, and proxy-based estimates of MAAT and MAP, the paleoenvironment is likely best-represented by either the "continental" or "semi-arid monsoonal" climates of Gallagher and Sheldon (2016). We note that the modern soil type for the settings of Gallagher and Sheldon (2016) consists of mollisols and thus may not be representative of the vertisols in which nodules used in this study formed. Their "continental" model indicates a decline in water storage in July/August which tends to bias carbonate formation to warmer values. In contrast, the "semi-arid monsoonal" model shows a decrease in water storage in April resulting in a slight cool season bias. However, cool season biases tend to be much smaller in magnitude (less than 4 ºC) than warm season biases (as much as 24 ºC) (Kelson et al., 2020). Therefore, regardless of the interpretation of seasonal biases, our mean temperature based on clumped isotopes (14.9 ºC) suggests very cool conditions in the mid-latitude Asian continental interior during the Aptian-Albian. Any potential warm season bias on our temperature results is unlikely as it would suggest even cooler conditions inconsistent with combined proxy observations. In addition, because soil carbonates likely form over long periods of time and are likely stabilized in the phreatic environment as the soil is removed from the active zone of pedogenesis, it is likely seasonal temperature biases are further dampened. Indeed, the temperatures calculated here are consistent with other regional paleotemperature proxy observations (e.g., Amiot et al., 2011), and counter to the predominantly warm greenhouse climate of the Cretaceous (Föllmi, 2012).

4.3 Latitudinal gradients of temperature and $\delta^{18}O_{mw}$ for the Aptian-Albian

Clumped isotope-based temperatures for the White Pagoda site indicate a mean record value of 14.9 ºC which is equivalent to $\delta^{18}O_P$-based temperature estimates (15 ºC) carried out on dinosaur teeth from formations within the same group (Xinminpu) in NW Asia (Amiot et al., 2011). The groundwater $\delta^{18}O$ based on our combined clumped isotope and carbonate isotope analyses range from −11.54 to −6.69‰ (VSMOW) and average −9.47‰, which is somewhat lower than the values of Amiot et al. (2011) (−7.0‰).

Modern climate observations of the study site indicate cool, dry conditions with mean $\delta^{18}O_{mw}$ of −9.31‰ and −7.66‰ in nearby Zhangye and Lanzhou, respectively (IAEA/WMO, 2020). Largely due to the influence of regional topography (study

location elevation: ~1500 m), present day precipitation averages < 100 mm/yr and MATs indicate locally cooler temperatures (9.0 ºC and 10.5 ºC in Zhangye and Lanzhou, respectively; IAEA/WMO, 2020) relative to global zonal averages (15.0 ºC; Rozanski et al., 1993). Aptian-Albian temperatures may similarly be influenced by regional paleotopography, though topographic reconstructions for Asia during the Aptian-Albian are lacking, limiting speculation.

410

Generally, proxy-based temperatures and $\delta^{18}O_{mw}$ for the Xinminpu Group tend to fall within zonally averaged general circulation GENESIS-MOM model results (Zhou et al., 2008) given the large range in possible site paleolatitude during the Aptian-Albian. For example, paleogeographic reconstructions indicate paleolatitudes ranging from ~35ºN to ~48ºN for the White Pagoda Site during the Aptian-Albian (Lin et al., 2003; Torsvik et al., 2012; Matthews et al., 2016), which

415 corresponds to simulated temperatures ranging from 9 to 19 ºC and simulated $\delta^{18}O_{mw}$ ranging from −11.8 to −6.7‰ (Zhou et al., 2008).

Combining our new temperature and $\delta^{18}O_{mw}$ data with that compiled in Amiot et al. (2011), we re-cast latitudinal temperature and $\delta^{18}O_{mw}$ gradients according to the paleogeography applied in Amiot et al. (2011) (Lin et al., 2003) and using

420 an updated paleogeography based on Matthews et al. (2016) (i.e., Gplates). The updated paleogeography results in higher Early Cretaceous paleolatitudes for all Asian sites included in this compilation (Supplementary Material; Table S5), including a more than +13ºN shift for the Xinminpu group sites (Fig. 6). When placed on the paleogeography of Lin et al. (2003), proxy-based temperature reconstructions for Asia indicate a cool climate relative to latitudinal models of temperature and hydrology (i.e., land surface gradients compiled in Suarez et al. (2011a) including: leaf physiognomy-based gradients of

425 Spicer and Corfield (1992), cool and warm Cretaceous gradients of Barron (1983), and GENESIS-MOM general circulation model gradients of Zhou et al. (2008)). For example, temperature data falls below even the coolest Cretaceous modeled gradient (i.e., Barron, 1983) despite agreement between proxy $\delta^{18}O_{mw}$ in mid-latitude continental Asia and the modeled cool Cretaceous (Fig. 7 panels a and b). However, if Matthews et al. (2016) paleolatitudes are applied, proxy-based temperatures become better aligned with Cretaceous modeled temperature gradients (Fig. 7 panel c). Additionally, the updated

430 paleolatitudes tend to offset $\delta^{18}O_p$-based $\delta^{18}O_{mw}$ estimates in a positive direction relative to the modeled cool Cretaceous $\delta^{18}O_{mw}$ gradient, aligning these data with a flatter, more modern appearing $\delta^{18}O_{mw}$ gradient (Fig. 7 panel d). Meanwhile, our clumped isotope and $\delta^{18}O_{carb}$-based $\delta^{18}O_{mw}$ value falls within error of the range in Cretaceous modeled $\delta^{18}O_{mw}$ gradients (Fig. 7 panel d) suggesting potential errors in required assumptions for $\delta^{18}O_p$-based $\delta^{18}O_{mw}$ reconstructions of Amiot et al. (2011). The $\delta^{18}O_p$ may be more ^{18}O-enriched compared to $\delta^{18}O_{mw}$ than accounted for in those original studies. The consumption of

435 evaporatively-enriched leaf water in herbivores provides one possible mechanism for $^{18}O_p$-enrichment (Levin et al., 2006). Alternatively, the range in paleolatitudes presented here demonstrate the large degree of uncertainty with regards to Early Cretaceous paleogeographic reconstructions of Asia (Supplementary Material; Table S5), which may be driving Aptian-Albian proxy-model disparities.

4.4 Atmospheric paleo-pCO$_2$

Cotton and Sheldon (2012) refine procedural guidelines previously established by Cerling and Quade (1993) and Ekart et al. (1999) for use of pedogenic carbonates in reconstructions of atmospheric pCO$_2$ which include maximum limits for Δ^{13}C (i.e., δ^{13}C$_{carb}$ $-$ δ^{13}C$_{org}$), isotopic heterogeneity and δ^{13}C versus δ^{18}O covariation. They suggest limiting proxy application to

445 samples with 14‰ < Δ^{13}C < 17‰ as modern soils with large Δ^{13}C tend to have S(z) values which fall off of the MAP versus S(z) relationship defined by Cotton and Sheldon (2012) and are likely to have been disproportionately influenced by atmospheric δ^{13}C. For our atmospheric pCO$_2$ reconstruction, we occluded samples with large Δ^{13}C (i.e., samples with Δ^{13}C > 18‰; sample 3B-021). We include two samples in our reconstruction (samples 6-003 and 4-038) which have 17‰ < Δ^{13}C < 18‰ (Table 1 and Fig. 5). Though this Δ^{13}C signature may indicate low-productivity (Cotton and Sheldon, 2012) which can

450 influence the MAP versus S(z) relationship, the presence of abundant root traces in sections 4 and 6 (i.e., Suarez et al., 2018) suggests otherwise. In addition to meeting Δ^{13}C criteria, no clear correlation between carbonate δ^{13}C and δ^{18}O is observed (Fig. 4) and carbonates tend to be isotopically homogeneous (Fig. 4; Table 4; maximum 1σ of 0.3‰ in all samples for both δ^{13}C and δ^{18}O). We include estimates of uncertainty in our atmospheric pCO$_2$ reconstructions following Retallack (2009). Specifically, uncertainty is equivalent to the square root of the sum of the individual components of uncertainty squared.

455 Here, we propagate uncertainty in δ^{13}C$_s$, including 2σ analytical uncertainty in δ^{13}C$_{carb}$ and 2σ temperature uncertainty, and δ^{13}C$_r$ (2σ analytical uncertainty). To test the sensitivity of S(z) estimates on pCO$_2$, we include two pCO$_2$ reconstructions using: 1) MAP-based variable S(z) computed for each sample following Cotton and Sheldon (2012), and 2) a large range in S(z), which is applied to all samples and propagated as additional uncertainty. For the second pCO$_2$ reconstruction approach, the maximum range in S(z) is set using the relationship of Cotton and Sheldon (2012), applying the maximum MAP value

460 observed in the sections containing samples for pCO$_2$ reconstruction (i.e., 984 mm/yr which translates to S(z) of 5309 ppmv). This maximum value is representative of some maximum modern S(z) values observed in Holocene calcic soils by Breecker et al. (2010) and consistent with summer minimum S(z) values observed in vertisol grasslands by Mielnick and Dugas (2000). Minimum S(z) is set at 2500 ppmv, following the recommended S(z) of Breecker et al. (2010), as this value is consistent with minimum MAP for our record following the relationship of Cotton and Sheldon (2012). As observed

465 previously for the Cretaceous (e.g., Franks et al., 2014), atmospheric paleo-pCO$_2$ derived from pedogenic carbonate stable isotopes tends to lose sensitivity at low atmospheric CO$_2$ concentrations resulting in calculated error which spans negative concentrations. Here, we exclude negative, unrealistic pCO$_2$ values from our record and report these minimums as 0 ppmv (Fig. 5) and note that calculated minimum pCO$_2$ is > $-$231 ppmv for all samples (Table 4).

470 Our atmospheric pCO$_2$ reconstruction suggests relatively low (for greenhouse climates) and variable pCO$_2$ over the study interval. This observation is consistent with cool Aptian-Albian temperatures (i.e., MAAT ~15 ºC in midlatitudes as indicated by this study and others). Mean atmospheric pCO$_2$ for the entire record is 396 ppmv and pCO$_2$ generally tracks temperature variability with low (i.e., < 300 ppmv) pCO$_2$ in the cool C10 interval ramping up section to ~1100 ppmv. Our

record is largely in agreement with paleobotanical proxy-based pCO$_2$ reconstructions for the Aptian-Albian, which range from ~500 to 1300 ppmv (Aucour et al., 2008; Passalia, 2009; Haworth et al., 2010; Du et al., 2016). While this study indicates slightly lower pCO$_2$ than other carbon-isotope based records for the Aptian-Albian (e.g., Ekart et al. (1999) suggest ~1500 ppmv; Wallmann (2001) suggest 700 to 1500 ppmv; Fletcher et al. (2005) suggest 1100 to 1200 ppmv), these records

490   do not all satisfy requirements of Cotton and Sheldon (2012) (e.g., $\Delta^{13}C < 17‰$ in the record of Ekart et al. (1999) likely biases to higher atmospheric pCO$_2$), and may lack the sampling resolution to pick up on shorter-term variations. Additionally, though comparatively offset to lower values, variability in our atmospheric pCO$_2$ reconstruction follows the pattern of Aptian-Albian pCO$_2$ variability observed in other pedogenic and pelagic marine carbonate-based estimates (i.e., gradual decrease in late Aptian with a low at the Aptian-Albian boundary before increasing into the early Albian; Li et al.,

495   2013; Bottini et al., 2015).

4.5 Aptian-Albian variations in atmospheric pCO$_2$, climate and the hydrologic cycle

Cooler midlatitude terrestrial temperatures (MAATs of ~15 ºC) are consistent with the post-OAE 1a "cold snap" hypothesis (e.g., Mutterlose et al., 2009) observed in terrestrial (e.g., Amiot et al., 2011) and sea surface temperature records (e.g., both nannofossil indicators and organic GDGT temperature proxy TEX$_{86}$ show cooling at globally distributed sites; Bottini et al.,

500   2015). Following Friedman and O'Neil (1977), coupled carbonate $\delta^{18}O$ and temperatures suggest variations in $\delta^{18}O_{mw}$ of ± 2.2‰ over the study interval consistent with shifts in the distribution of atmospheric moisture associated with climate change, but similar in magnitude to 2σ reconstruction uncertainty (Table 2). However, climate change-induced variations in Asian continental interior $\delta^{18}O_{mw}$ during the early Cretaceous would be expected given model results which show shifts in $\delta^{18}O_{mw}$ of +2 to +4‰ associated with two doublings of atmospheric pCO$_2$ (global average surface warming of 6 ºC) in

505   continental interiors (Poulsen et al., 2007). Our records similarly suggest subtle warming-induced ^{18}O-enrichment in $\delta^{18}O_{mw}$ for continental Asia, as atmospheric pCO$_2$, temperature and $\delta^{18}O_{mw}$ increase following the C10 interval (Fig. 5). Variability in $\delta^{18}O_{mw}$ is likely minimally influenced by seasonality following our interpretation above of consistent seasonal formation of pedogenic carbonate nodules in vertisols. While age controls are limited, chemostratigraphic correlations (i.e., Suarez et al., 2018) suggest our record spans several Myr (i.e., C7 to C12 carbon isotope segments after Menegatti et al. (1998) and

510   Bralower et al. (1999); roughly 6 million years). Given the temporal coarseness of our record which likely does not pick up on peak temperature variability, we observe subtle temperature shifts over the interval (i.e., cooling of −2 to −4 °C preceding +4 to +6 °C of warming across the inferred C10 interval), which likely corresponds to the cool interval between OAE 1a and OAE 1b and may include Kilian and/or OAE 1b warmth (e.g., Bottini et al., 2015) around 140 m (Fig. 5).

515   Shifts in the hydrologic cycle reflected in $\delta^{18}O_{mw}$ and MAP (Fig. 5) track Δ_{47}-based temperatures, suggesting climate-controlled regional shifts in interior Asian hydrologic cycle. Interestingly, the driest conditions tend to correlate to relative lows in temperature and $\delta^{18}O_{mw}$ perhaps pointing to variations in the seasonality and/or sourcing of meteoric waters in Asia associated with long-term climate evolution. Compared with background environmental conditions, cooler temperatures

525 (down to 11.1 °C), drier conditions (MAP < 600 mm/yr), and ^{18}O-depleted meteoric waters are observed in the C10 interval, consistent with models of precipitation change for the mid-Cretaceous (e.g., Poulsen et al., 2007) and observations of more widespread dry conditions in Asia during cool Cretaceous intervals (e.g., Hasegawa et al., 2012).

Hasegawa et al. (2012) used sedimentological records from Asia to help constrain potential shifts in the descending limb of
530 the Hadley cell related to Cretaceous climate change and compared these observations to of Hadley cell circulation simulations, concluding that as paleo-pCO$_2$ concentration increases, so does the width of the Hadley Cell, but that at ~1000 ppmv paleo-pCO$_2$ and greater, the descending limb of the Hadley cell contracts from 30ºN and ºS to 15ºN and ºS reorganizing the distribution of atmospheric water vapor. This hypothesis is further supported by paleoenvironmental observations (i.e., shifts in lithology and climate-sensitive fossils associated with changes in aridity; Chumakov et al., 1995;
535 Chumakov, 2004), and general circulation models which indicate a 30ºN position of the descending limb of the Hadley cell during Cretaceous greenhouse warmth (Floegel, 2001). The time bins that Hasegawa et al. (2012) investigates are larger than the interval investigated here, but the shifts in atmospheric pCO$_2$ encompass the range of hypothesized thresholds for shifts in Hadley Cell circulation. The relatively cool and dry conditions and ^{18}O-depleted meteoric waters during the C10 interval (potentially associated with the "cold snap"; Mutterlose et al., 2009) may reflect on a shift in climate and Hadley cell
540 circulation, driven by a decrease in atmospheric pCO$_2$ (e.g., Hasegawa et al., 2012). Indeed, other sedimentological evidence (e.g., glendonites) provide further support for relatively cold conditions at high northern latitudes associated with this interval (Vickers et al., 2019). For our records, atmospheric pCO$_2$ drops during the C10 interval from pre- and post-segment values within error of 1000 ppmv, to < 350 ppmv in the C10 interval (Fig. 5; Table 4), well below the critical threshold proposed by Hasegawa et al. (2012). It is important to note that the decrease in atmospheric pCO$_2$ observed in our record is
545 similar in magnitude to the error associated with the reconstruction, and while declining pCO$_2$ is consistent with cooling during the C10 interval, more chronologic work is needed to constrain the timing and complete magnitude of pCO$_2$ variability across the Aptian-Albian along with wider spatial quantitative paleoclimate proxies. Generally, however, as atmospheric pCO$_2$ increases from the low in the C10 interval to a peak just after, precipitation and temperature increase, consistent with the proposed climate shifts that Hasegawa et al. (2012) suggest, in a "supergreenhouse" mode. Variability in
550 δ^{18}O$_{mw}$ and MAP is observed throughout our study interval, however, which is consistent with either multiple fluctuations in Hadley cell circulation across the interval or, more likely, background regional variability in the early Cretaceous hydrologic cycle in continental interior Asia.

5 Conclusions

In summary, new continental Asia midlatitude multi-proxy records of Aptian-Albian carbon cycle, climate and hydrologic
555 cycle suggest cool conditions in early Cretaceous midlatitudes (mean of 14.9 ºC; 35ºN to 48ºN paleolatitude depending on applied paleogeographic reconstruction) relative to background Cretaceous greenhouse warmth, consistent with our

estimated atmospheric pCO$_2$ (mean value of 396 ppmv) calculated using carbon isotopes in pedogenic carbonates and previous regional MAAT observations (Amiot et al., 2011). Variations in the hydrologic cycle (i.e., decreases in MAP and δ^{18}O$_{mw}$) are associated with transient cooling (-2 to -4 ºC) during the C10 carbon isotope high, consistent with general circulation models which suggest differences in temperature, MAP and δ^{18}O$_{mw}$ similar in magnitude to our observations associated with one to two doubling(s) (or in terms of cooling, halving(s)) of atmospheric pCO$_2$. These new paleoclimate parameters may be useful to future climate modeling efforts and for understanding potential variability (cooling and warming; shifts in precipitation) in an otherwise greenhouse climate.

Acknowledgments

We are grateful to Bruce Barnett for discussion and analytical assistance in the KPESIL at KU, and Katie Snell and Brett Davidheiser-Kroll for discussion, access and assistance in the CUBES-SIL at CUB for clumped isotope analyses. Thank you to Greg Ludvigson for help with cathodoluminescence and lively discussion. This manuscript was greatly improved by reviews from two anonymous reviewers and CL feedback from Hilary Corlett. This work was supported by the National Science Foundation (grants NSF EAR1941017 to M. Suarez and NSF EAR1024671 to P. Dodson), and grants to H. You from The Strategic Priority Research Program of Chinese Academy of Sciences (grant XDB260000000) and National Natural Science Foundation of China (grants 41688103 and 41872021).

Data Availability

All new data reported herein can be found in the tables, Supplementary Material and Open Science Framework (Harper et al., 2020; DOI: 10.17605/OSF.IO/ZUYHN).

References

Amante, C., and Eakins, B. W.: ETOPO1 arc-minute global relief model: procedures, data sources and analysis, NOAA Technical Memorandum, 2009.

Amiot, R., Lécuyer, C., Buffetaut, E., Fluteau, F., Legendre, S., and Martineau, F.: Latitudinal temperature gradient during the Cretaceous Upper Campanian–Middle Maastrichtian: δ18O record of continental vertebrates, Earth and Planetary Science Letters, 226, 255-272, 10.1016/j.epsl.2004.07.015, 2004.

Amiot, R., Wang, X., Zhou, Z., Wang, X., Buffetaut, E., Lecuyer, C., Ding, Z., Fluteau, F., Hibino, T., Kusuhashi, N., Mo, J., Suteethorn, V., Wang, Y., Xu, X., and Zhang, F.: Oxygen isotopes of East Asian dinosaurs reveal exceptionally cold Early Cretaceous climates, Proc Natl Acad Sci U S A, 108, 5179-5183, 10.1073/pnas.1011369108, 2011.

Ando, A., Kakegawa, T., Takashima, R., and Saito, T.: New perspective on Aptian carbon isotope stratigraphy: data from δ13C records pf terrestrial organic matter, Geology, 30, 4, 2002.

Aucour, A.-M., Gomez, B., Sheppard, S. M. F., and Thévenard, F.: δ13C and stomatal number variability in the Cretaceous conifer Frenelopsis, Palaeogeography, Palaeoclimatology, Palaeoecology, 257, 462-473, 10.1016/j.palaeo.2007.10.027, 2008.

595   Barron, E. J.: A warm, equable Cretaceous: The nature of the problem, Earth-Science Reviews, 19, 34, 1983.

Bernasconi, S. M., Daëron, M., Bergmann, K., Bonifacie, M., Meckler, A. N., and al., e.: InterCarb: A community effort to improve inter-laboratory standardization of the carbonate clumped isotope thermometer using carbonate standards. , Open Archive ESSOAr, doi.org/10.1002/essoar.10504430.4, 2021.

Birkeland, P. W., Miller, D. C., Patterson, P. E., Price, A. B., and Shroba, R. R.: Soil-geomorphic relationships near Rocky
600   Flats, Boulder and Golden, Colorado area, with a stop at the pre-fountain formation paleosol of Wahlstrom (1948), Geologic Society of America Trip, 18, 13, 1999.

Bonifacie, M., Calmels, D., Eiler, J. M., Horita, J., Chaduteau, C., Vasconcelos, C., Agrinier, P., Katz, A., Passey, B. H., Ferry, J. M., and Bourrand, J.-J.: Calibration of the dolomite clumped isotope thermometer from 25 to 350 °C, and implications for a universal calibration for all (Ca, Mg, Fe)CO3 carbonates, Geochimica et Cosmochimica Acta, 200, 255-
605   279, 10.1016/j.gca.2016.11.028, 2017.

Bottini, C., Erba, E., Tiraboschi, D., Jenkyns, H. C., Schouten, S., and Sinninghe Damsté, J. S.: Climate variability and ocean fertility during the Aptian Stage, Climate of the Past, 11, 383-402, 10.5194/cp-11-383-2015, 2015.

Bralower, T. J., CoBabe, E., Clement, B., Sliter, W. V., Osburn, C. L., and Longoria, J.: The record of global change in mid-Cretaceous (Barremian-Albian) sections from the Sierra Madre, Northeastern Mexico, Journal of Foraminiferal Research,
610   29, 20, 1999.

Brand, W. A., Assonov, S. S., and Coplen, T. B.: Correction for the 17O interference in δ(13C) measurements when analyzing CO2 with stable isotope mass spectrometry (IUPAC Technical Report), Pure and Applied Chemistry, 82, 1719-1733, 10.1351/pac-rep-09-01-05, 2010.

Breecker, D. O., Sharp, Z. D., and McFadden, L. D.: Seasonal bias in the formation and stable isotopic composition of
615   pedogenic carbonate in modern soils from central New Mexico, USA, Geological Society of America Bulletin, 121, 630-640, 10.1130/b26413.1, 2009.

Breecker, D. O., Sharp, Z. D., and McFadden, L. D.: Atmospheric CO2 concentrations during ancient greenhouse climates were similar to those predicted for A.D. 2100, Proc Natl Acad Sci U S A, 107, 576-580, 10.1073/pnas.0902323106, 2010.

Burgener, L., Hyland, E., Huntington, K. W., Kelson, J. R., and Sewall, J. O.: Revisiting the equable climate problem during
620   the Late Cretaceous greenhouse using paleosol carbonate clumped isotope temperatures from the Campanian of the Western Interior Basin, USA, Palaeogeography, Palaeoclimatology, Palaeoecology, 516, 244-267, 10.1016/j.palaeo.2018.12.004, 2019.

Carmichael, M. J., Lunt, D. J., Huber, M., Heinemann, M., Kiehl, J., LeGrande, A., Loptson, C. A., Roberts, C. D., Sagoo, N., Shields, C., Valdes, P. J., Winguth, A., Winguth, C., and Pancost, R. D.: Insights into the early Eocene hydrological
625   cycle from an ensemble of atmosphere–ocean GCM simulations, Climate of the Past Discussions, 11, 3277-3339, 10.5194/cpd-11-3277-2015, 2015.

Cazenave, S., Chapoulie, R., and Villeneuve, G.: Cathodoluminescence of synthetic and natural calcite: the effects of manganese and iron on orange emission, Mineralogy and Petrology, 78, 11, 2003.

Cerling, T. E.: Carbon dioxide in the atmosphere: Evidence from Cenozoic and Mesozoic paleosols, American Journal of
630   Science, 291, 10.2475/ajs.291.4.377, 1991.

Cerling, T. E., and Quade, J.: Stable Carbon and Oxygen Isotopes in Soil Carbonates, Climate Change in Continental
Isotopic Records, 78, 1993.

Chen, J., and Yang, H.: Geological development of the northwest China basins during the Mesozoic and Ceonzoic,
Phanerozoic Geology of Northwest China 1996.

635   Chumakov, N. M., Zharkov, M. A., Herman, A. B., D'oludenko, M. P., Kalandadze, N. N., Lebedev, E. L., Ponomarenko,
A. G., and Rautian, A. S.: Climatic belts of the mid-Cretaceous time, Stratigraphy and Geological Correlation, 3, 22, 1995.

Chumakov, N. M.: Climatic zones and climate of the Cretaceous period, in: Climate in the epochs of major biospheric
transformations, edited by: Sciences, T. o. t. G. I. o. t. R. A. o., Moscow, 19, 2004.

Cotton, J. M., and Sheldon, N. D.: New constraints on using paleosols to reconstruct atmospheric pCO_2, Geological Society
640   of America Bulletin, 124, 1411-1423, 10.1130/b30607.1, 2012.

Daëron, M., Blamart, D., Peral, M., and Affek, H. P.: Absolute isotopic abundance ratios and the accuracy of Δ47
measurements, Chemical Geology, 442, 83-96, 10.1016/j.chemgeo.2016.08.014, 2016.

Dennis, K. J., Affek, H. P., Passey, B. H., Schrag, D. P., and Eiler, J. M.: Defining an absolute reference frame for 'clumped'
isotope studies of CO_2, Geochimica et Cosmochimica Acta, 75, 7117-7131, 10.1016/j.gca.2011.09.025, 2011.

645   Driese, S. D., and Mora, C. I.: Physico-chemical environment of pedogenic carbonate formation in Devonian vertic
palaeosols, central Appalachians, USA, Sedimentology, 40, 18, 1993.

Du, B., Sun, B., Zhang, M., Yang, G., Xing, L., Tang, F., and Bai, Y.: Atmospheric palaeo-CO_2 estimates based on the
carbon isotope and stomatal data of Cheirolepidiaceae from the Lower Cretaceous of the Jiuquan Basin, Gansu Province,
Cretaceous Research, 62, 142-153, 10.1016/j.cretres.2015.07.020, 2016.

650   Du, B., Lei, X., Zhang, M., Wang, S., Li, A., Du, Z., and Xing, W.: Late Early Cretaceous climate and pCO_2 estimates in
the Liupanshan Basin, Northwest China, Palaeogeography, Palaeoclimatology, Palaeoecology, 503, 26-39,
10.1016/j.palaeo.2018.04.023, 2018.

Ekart, D. D., Cerling, T. E., Montanez, I. P., and Tabor, N., J,: A 400 million year carbon isotope record of pedogenic
carbonate: Implications for paleoatmospheric carbon dioxide, American Journal of Science, 299, 23, 1999.

655   Fernandez, A., Müller, I. A., Rodríguez-Sanz, L., van Dijk, J., Looser, N., and Bernasconi, S. M.: A Reassessment of the
Precision of Carbonate Clumped Isotope Measurements: Implications for Calibrations and Paleoclimate Reconstructions,
Geochemistry, Geophysics, Geosystems, 18, 4375-4386, 10.1002/2017gc007106, 2017.

Fletcher, B. J., Beerling, D. J., Brentnall, S. J., and Royer, D. L.: Fossil bryophytes as recorders of ancient CO_2 levels:
Experimental evidence and a Cretaceous case study, Global Biogeochemical Cycles, 19, 10.1029/2005gb002495, 2005.

660   Floegel, S.: On the influence of precessional Milankovitch cycles on the Late Cretaceous climate system: comparison of
GCM- results, geochemical, and sedimentary proxies for the Western Interior Seaway of North America, Faculty of
Mathematics and Natural Sciences, Christian-Albrecht's- University, Kiel, Germany, 236 pp., 2001.

Föllmi, K. B.: Early Cretaceous life, climate and anoxia, Cretaceous Research, 35, 230-257, 10.1016/j.cretres.2011.12.005, 2012.

665 Franks, P. J., Royer, D. L., Beerling, D. J., Van de Water, P. K., Cantrill, D. J., Barbour, M. M., and Berry, J. A.: New constraints on atmospheric CO2concentration for the Phanerozoic, Geophysical Research Letters, 41, 4685-4694, 10.1002/2014gl060457, 2014.

Friedman, I., and O'Neil, J. R.: Compilation of stable isotope fractionation factors of geochemical interest, in: Data of Geochemistry, 6 ed., edited by: Fleischer, M., US Government Printing Office, 1977.

670 Gallagher, T. M., and Sheldon, N. D.: Combining soil water balance and clumped isotopes to understand the nature and timing of pedogenic carbonate formation, Chemical Geology, 435, 79-91, 10.1016/j.chemgeo.2016.04.023, 2016.

Ghosh, P., Adkins, J., Affek, H., Balta, B., Guo, W., Schauble, E. A., Schrag, D., and Eiler, J. M.: 13C–18O bonds in carbonate minerals: A new kind of paleothermometer, Geochimica et Cosmochimica Acta, 70, 1439-1456, 10.1016/j.gca.2005.11.014, 2006.

675 Habermann, D., Neuser, R. D., and Richter, D. K.: Quantitative High Resolution Spectral Analysis of Mn2+ in Sedimentary Calcite, in: Cathodoluminescence in Geosciences, Springer, 331-358, 2000.

Harper, D. T., Suarez, M. B., Uglesich, J., You, H., Li, D., and Dodson, P.: Aptian-Albian clumped isotopes from northwest China: Cool temperatures, variable atmospheric pCO2 and regional shifts in hydrologic cycle, Open Science Framework 10.17605/OSF.IO/ZUYHN, 2020.

680 Hasegawa, H., Imsamut, S., Charusiri, P., Tada, R., Horiuchi, Y., and Hisada, K.-I.: 'Thailand was a desert' during the mid-Cretaceous: Equatorward shift of the subtropical high-pressure belt indicated by eolian deposits (Phu Thok Formation) in the Khorat Basin, northeastern Thailand, Island Arc, 19, 605-621, 10.1111/j.1440-1738.2010.00728.x, 2010.

Hasegawa, H., Tada, R., Jiang, X., Suganuma, Y., Imsamut, S., Charusiri, P., Ichinnorov, N., and Khand, Y.: Drastic shrinking of the Hadley circulation during the mid-Cretaceous Supergreenhouse, Climate of the Past, 8, 1323-1337, 685 10.5194/cp-8-1323-2012, 2012.

Haworth, M., Heath, J., and McElwain, J. C.: Differences in the response sensitivity of stomatal index to atmospheric CO2 among four genera of Cupressaceae conifers, Ann Bot, 105, 411-418, 10.1093/aob/mcp309, 2010.

Hay, W. W.: Toward understanding Cretaceous climate—An updated review, Science China Earth Sciences, 60, 5-19, 10.1007/s11430-016-0095-9, 2016.

690 Heimhoffer, U., Hochuli, P. A., Burla, S., Andersen, N., and H., W.: Terrestrial carbon-isotope records from coastal deposits (Algarve, Portugal): a tool for chemostratitgraphic correlation on an intrabasinal and global scale, Terra Nova, 15, 6, 2003.

Hönisch, B., Ridgwell, A., Schmidt, D. N., Thomas, E., Gibbs, S. J., Sluijs, A., Zeebe, R., Kump, L., Martindale, R. C., Greene, S. E., Kiessling, W., Ries, J., Zachos, J. C., Royer, D. L., Barker, S., Marchitto, T. M., Jr., Moyer, R., Pelejero, C., Ziveri, P., Foster, G. L., and Williams, B.: The geological record of ocean acidification, Science, 335, 1058-1063, 695 10.1126/science.1208277, 2012.

Jenkyns, H. C.: Transient cooling episodes during Cretaceous Oceanic Anoxic Events with special reference to OAE 1a (Early Aptian), Philos Trans A Math Phys Eng Sci, 376, 10.1098/rsta.2017.0073, 2018.

Kelson, J. R., Huntington, K. W., Breecker, D. O., Burgener, L. K., Gallagher, T. M., Hoke, G. D., and Petersen, S. V.: A proxy for all seasons? A synthesis of clumped isotope data from Holocene soil carbonates, Quaternary Science Reviews,
700 234, 10.1016/j.quascirev.2020.106259, 2020.

Kuang, H. W., Liu, Y. Q., Liu, Y. X., Peng, N., Xu, H., and Dong, C.: Stratigraphy and depositional palaeogeography of the Early Cretaceous basins in Da Hinggan Mountains–Mongolia orogenic belt and its neighboring areas, Geological Bulletin of China 32, 22, 2013.

Levin, N. E., Cerling, T. E., Passey, B. H., Harris, J. M., and Ehleringer, J. R.: A stable isotope aridity index for terrestrial
705 environments, Proc Natl Acad Sci U S A, 103, 11201-11205, 10.1073/pnas.0604719103, 2006.

Li, X., Xu, W., Liu, W., Zhou, Y., Wang, Y., Sun, Y., and Liu, L.: Climatic and environmental indications of carbon and oxygen isotopes from the Lower Cretaceous calcrete and lacustrine carbonates in Southeast and Northwest China, Palaeogeography, Palaeoclimatology, Palaeoecology, 385, 171-189, 10.1016/j.palaeo.2013.03.011, 2013.

Lin, W., Chen, Y., Faure, M., and Wang, Q.: Tectonic implications of new Late Cretaceous paleomagnetic constraints from
710 Eastern Liaoning Peninsula, NE China, Journal of Geophysical Research: Solid Earth, 108, 10.1029/2002jb002169, 2003.

Ludvigson, G. A., Joeckel, R. M., Gonzalez, L. A., Gulbranson, E. L., Rasbury, E. T., Hunt, G. J., Kirkland, J. I., and Madsen, S.: Correlation of Aptian-Albian Carbon Isotope Excursions in Continental Strata of the Cretaceous Foreland Basin, Eastern Utah, U.S.A, Journal of Sedimentary Research, 80, 955-974, 10.2110/jsr.2010.086, 2010.

Ludvigson, G. A., Joeckel, R. M., Murphy, L. R., Stockli, D. F., González, L. A., Suarez, C. A., Kirkland, J. I., and Al-
715 Suwaidi, A.: The emerging terrestrial record of Aptian-Albian global change, Cretaceous Research, 56, 1-24, 10.1016/j.cretres.2014.11.008, 2015.

Matthews, K. J., Maloney, K. T., Zahirovic, S., Williams, S. E., Seton, M., and Müller, R. D.: Global plate boundary evolution and kinematics since the late Paleozoic, Global and Planetary Change, 146, 226-250, 10.1016/j.gloplacha.2016.10.002, 2016.

720 Menegatti, A. P., Weissert, H., Brown, R. S., Tyson, R. V., Farrimond, P., Strasser, A., and Caron, M.: High-resolution δ13C stratigraphy through the Early Aptian "Livello selli" of the Alpine tethys, Paleoceanography, 13, 530-545, 10.1029/98pa01793, 1998.

Mielnick, P. C., and Dugas, W. A.: Soil CO2 flux in a tallgrass prairie, Soil Biology and Biochemistry, 32, 8, 2000.

Mintz, J. S., Driese, S. G., Breecker, D. O., and Ludvigson, G. A.: Influence of Changing Hydrology on Pedogenic Calcite
725 Precipitation in Vertisols, Dance Bayou, Brazoria County, Texas, U.S.A.: Implications for Estimating Paleoatmospheric PCO2, Journal of Sedimentary Research, 81, 394-400, 10.2110/jsr.2011.36, 2011.

Mutterlose, J., Bornemann, A., and Herrle, J.: The Aptian – Albian cold snap: Evidence for "mid" Cretaceous icehouse interludes, Neues Jahrbuch für Geologie und Paläontologie - Abhandlungen, 252, 217-225, 10.1127/0077-7749/2009/0252-0217, 2009.

730 Nordt, L. C., and Driese, S. D.: New weathering index improves paleorainfall estimates from Vertisols, Geology, 38, 407-410, 10.1130/g30689.1, 2010.

Passalia, M. G.: Cretaceous pCO2 estimation from stomatal frequency analysis of gymnosperm leaves of Patagonia, Argentina, Palaeogeography, Palaeoclimatology, Palaeoecology, 273, 8, 2009.

Passey, B. H., Levin, N. E., Cerling, T. E., Brown, F. H., and Eiler, J. M.: High-temperature environments of human
735   evolution in East Africa based on bond ordering in paleosol carbonates, Proc Natl Acad Sci U S A, 107, 11245-11249,
10.1073/pnas.1001824107, 2010.

Petersen, S. V., Defliese, W. F., Saenger, C., Daëron, M., Huntington, K. W., John, C. M., Kelson, J. R., Bernasconi, S. M.,
Colman, A. S., Kluge, T., Olack, G. A., Schauer, A. J., Bajnai, D., Bonifacie, M., Breitenbach, S. F. M., Fiebig, J.,
Fernandez, A. B., Henkes, G. A., Hodell, D., Katz, A., Kele, S., Lohmann, K. C., Passey, B. H., Peral, M. Y., Petrizzo, D.
740   A., Rosenheim, B. E., Tripati, A., Venturelli, R., Young, E. D., and Winkelstern, I. Z.: Effects of Improved 17O Correction
on Interlaboratory Agreement in Clumped Isotope Calibrations, Estimates of Mineral-Specific Offsets, and Temperature
Dependence of Acid Digestion Fractionation, Geochemistry, Geophysics, Geosystems, 10.1029/2018gc008127, 2019.

Poulsen, C. J., Pollard, D., and White, T. S.: General circulation model simulation of the δ18O content of continental
precipitation in the middle Cretaceous: A model-proxy comparison, Geology, 35, 10.1130/g23343a.1, 2007.

745   Retallack, G. J.: Colour guide to paleosols, edited by: Ltd., J. W. a. S., 1997.

Retallack, G. J.: Refining a pedogenic-carbonate CO2 paleobarometer to quantify a middle Miocene greenhouse spike,
Palaeogeography, Palaeoclimatology, Palaeoecology, 281, 57-65, 10.1016/j.palaeo.2009.07.011, 2009.

Romanek, C. S., Grossman, E. L., and Morse, J. W.: Carbon isotopic fractionation in synthetic aragonite and calcite: effects
of temperature and precipitation rate, Geochimica et Cosmochimica Acta, 56, 12, 1992.

750   Rozanski, K., Luis, A., and Roberto, G.: Isotopic patterns in modern global precipitation, in: Climate Change in Continental
Isotopic Records, edited by: Swart, P. K., Lohmann, K. C., Mckenzie, J., and Savin, S., Geophysical Monograph Series,
American Geophysical Union, 1993.

Schauble, E. A., Ghosh, P., and Eiler, J. M.: Preferential formation of 13C–18O bonds in carbonate minerals, estimated
using first-principles lattice dynamics, Geochimica et Cosmochimica Acta, 70, 2510-2529, 10.1016/j.gca.2006.02.011, 2006.

755   Schauer, A. J., Kelson, J., Saenger, C., and Huntington, K. W.: Choice of (17) O correction affects clumped isotope
(Delta47) values of CO2 measured with mass spectrometry, Rapid Commun Mass Spectrom, 30, 2607-2616,
10.1002/rcm.7743, 2016.

Sheldon, N. D., and Tabor, N. J.: Quantitative paleoenvironmental and paleoclimatic reconstruction using paleosols, Earth-
Science Reviews, 95, 1-52, 10.1016/j.earscirev.2009.03.004, 2009.

760   Spicer, R. A., and Corfield, R. M.: A review of terrestrial and marine climates in the Cretaceous with implications for
modelling the 'Greenhouse Earth', Geol. Mag., 129, 12, 1992.

Suarez, C. A., Gonzalez, L. A., Ludvigson, G. A., Kirkland, J. I., Cifelli, R. L., and Kohn, M. J.: Multi-Taxa Isotopic
Investigation of Paleohydrology In the Lower Cretaceous Cedar Mountain Formation, Eastern Utah, U.S.A.: Deciphering
Effects Of the Nevadaplano Plateau On Regional Climate, Journal of Sedimentary Research, 84, 975-987,
765   10.2110/jsr.2014.76, 2014.

Suarez, M. B., González, L. A., and Ludvigson, G. A.: Quantification of a greenhouse hydrologic cycle from equatorial to
polar latitudes: The mid-Cretaceous water bearer revisited, Palaeogeography, Palaeoclimatology, Palaeoecology, 307, 301-
312, 10.1016/j.palaeo.2011.05.027, 2011a.

Suarez, M. B., Passey, B. H., and Kaakinen, A.: Paleosol carbonate multiple isotopologue signature of active East Asian
770   summer monsoons during the late Miocene and Pliocene, Geology, 39, 1151-1154, 10.1130/g32350.1, 2011b.

Suarez, M. B., Milder, T., Peng, N., Suarez, C. A., You, H., Li, D., and Dodson, P.: Chemostratigraphy of the Lower Cretaceous dinosaur-bearing Xiagou and Zhonggou Formations, Yujingzi Basin, Northwest China, Journal of Vertebrate Paleontology, 38, 10.1080/02724634.2017.1510412, 2018.

775   Tabor, C. R., Poulsen, C. J., Lunt, D. J., Rosenbloom, N. A., Otto-Bliesner, B. L., Markwick, P. J., Brady, E. C., Farnsworth, A., and Feng, R.: The cause of Late Cretaceous cooling: A multimodel-proxy comparison, Geology, 44, 4, 2016.

Tabor, N. J., and Myers, T. S.: Paleosols as Indicators of Paleoenvironment and Paleoclimate, Annual Review of Earth and Planetary Sciences, 43, 333-361, 10.1146/annurev-earth-060614-105355, 2015.

Torsvik, T. H., VanderVoo, R., Preeden, U., MacNiocaill, C., Steinberger, B., Doubrovine, P. V., vanHinsbergen, D. J. J., Domeier, M., Gaina, C., Tovher, E., Meert, J. G., McCausland, P. J., and Cocks, L. R. M.: Phanerozoic polar wander,
780   paleogeography and dynamics, Earth-Science Reviews, 114, 44, 2012.

Vickers, M. L., Price, G. D., Jerrett, R. M., Sutton, P., Watkinson, M. P., and FitzPatrick, M.: The duration and magnitude of Cretaceous cool events: Evidence from the northern high latitudes, GSA Bulletin, 131, 1979-1994, 10.1130/b35074.1, 2019.

Vincent, S. J., and Allen, M. B.: Evolution of the Minle and Chaoshui Bains, China: Implications for Mesozoic strike-slip basin formation in Central Asia, GSA Bulletin, 111, 18, 1999.

785   Wallmann, K.: Controls on the Cretaceous and Cenozoic evolution of seawater composition, atmospheric CO2 and climate, Geochimica et Cosmochimica Acta, 65, 21, 2001.

White, T. S., González, L. A., Ludvigson, G. A., and Poulsen, C. J.: Middle Cretaceous greenhouse hydrologic cycle of North America, Geology, 29, 4, 2001.

Zachos, J. C., Dickens, G. R., and Zeebe, R. E.: An early Cenozoic perspective on greenhouse warming and carbon-cycle
790   dynamics, Nature, 451, 279-283, 10.1038/nature06588, 2008.

Zeebe, R. E.: LOSCAR: Long-term Ocean-atmosphere-Sediment CArbon cycle Reservoir Model v2.0.4, Geoscientific Model Development, 5, 149-166, 10.5194/gmd-5-149-2012, 2012.

Zheng, D., Wang, H., Li, S., Wang, B., Jarzembowski, E. A., Dong, C., Fang, Y., Teng, X., Yu, T., Yang, L., Li, Y., Zhao, X., Xue, N., Chang, S.-C., and Zhang, H.: Synthesis of a chrono- and biostratigraphical framework for the Lower Cretaceous
795   of Jiuquan, NW China: Implications for major evolutionary events, Earth-Science Reviews, 213, 10.1016/j.earscirev.2020.103474, 2021.

Zhou, J., Poulsen, C. J., Pollard, D., and White, T. S.: Simulation of modern and middle Cretaceous marineδ18O with an ocean-atmosphere general circulation model, Paleoceanography, 23, n/a-n/a, 10.1029/2008pa001596, 2008.

Zhou, J., and Chafetz, H. S.: Biogenic caliches in Texas: The role of organisms and effect of climate, Sedimentary Geology,
800   222, 207-225, 10.1016/j.sedgeo.2009.09.003, 2009.
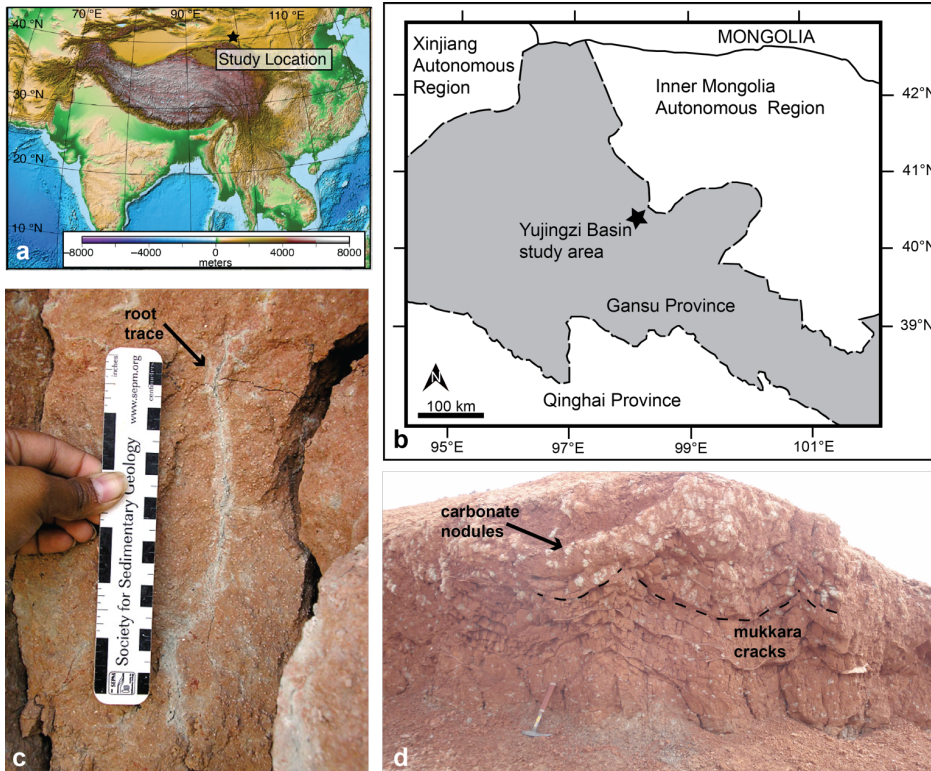
805 **Figure 1.** Approximate location of sampled sections with respect to regional topography (panel a; Amante and Eakins, 2009) and geography (panel b). Outcrop images of carbonate nodule bearing vertisol section typical of the composite study section (panels c and d). Root traces, mukkara cracks, ped structure, and coloration (Retallack, 1997) are all indicative of vertisols.

Deleted: Field map showing locations of

Deleted: measured

Deleted: (circles) and nearby faunal localities (bone

Deleted: symbol) on aerial photography from © Google Earth. Regional modern topographic map of Asia (

Deleted: inset with study location noted.
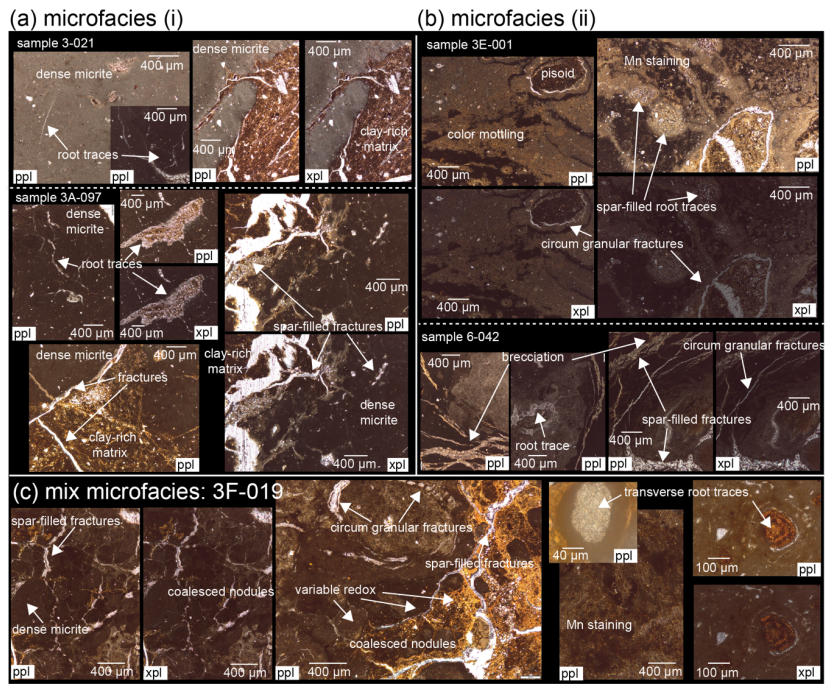
815 **Figure 2. Annotated photomicrographs from select carbonate nodules of the White Pagoda Site. Samples are split into two microfacies (panels a and b) with sample 3F-019 appearing to be a mixture of the two microfacies (panel c).**
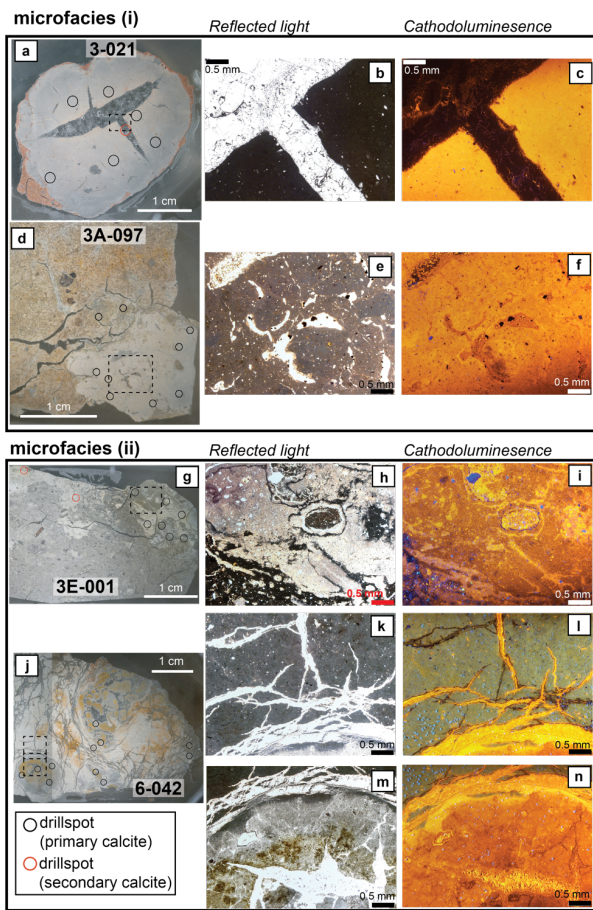
Figure 3. Reflected light (left column), transmitted light (middle column) and cathodoluminesence (CL; right column) images of select nodule thin sections (two from each microfacies group; top two samples are microfacies (i) and bottom two samples are microfacies (ii)). Samples 3-021 (panels a-c), 3A-097 (panels d-f), 3E-001 (panels g-i), and 6-042 (panels j-m) are included. Drillspots for δ^{13}C and δ^{18}O analysis, mapped from billets, are indicated by circles. Dashed squares are the approximate field of view for transmitted light and CL images.
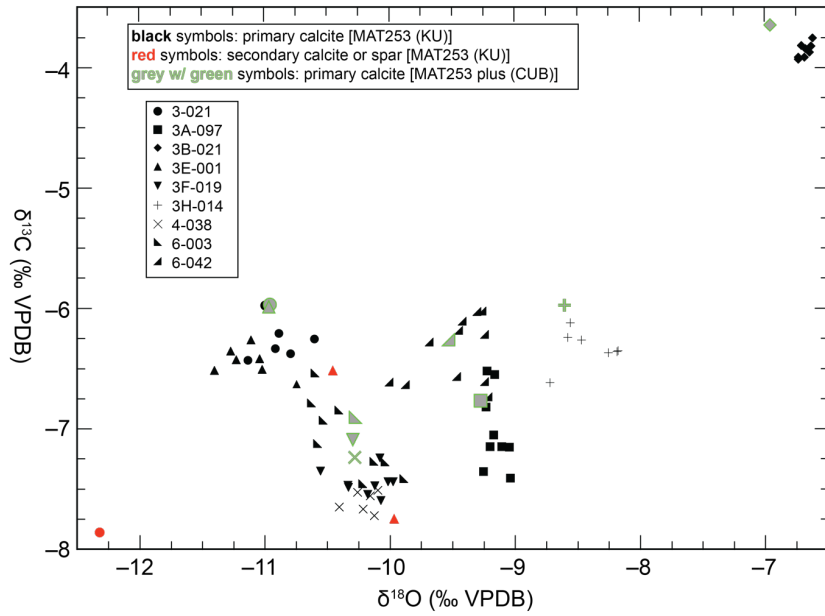
825 **Figure 4. Carbonate δ¹³C and δ¹⁸O for White Pagoda samples. Black symbols represent drillspot measurements of inferred primary calcite and red symbols represent drillspot measurements of inferred secondary calcite (measured at KU). Grey with green symbols represent mean δ¹³C and δ¹⁸O measured on larger inferred primary calcite samples at CUB.**
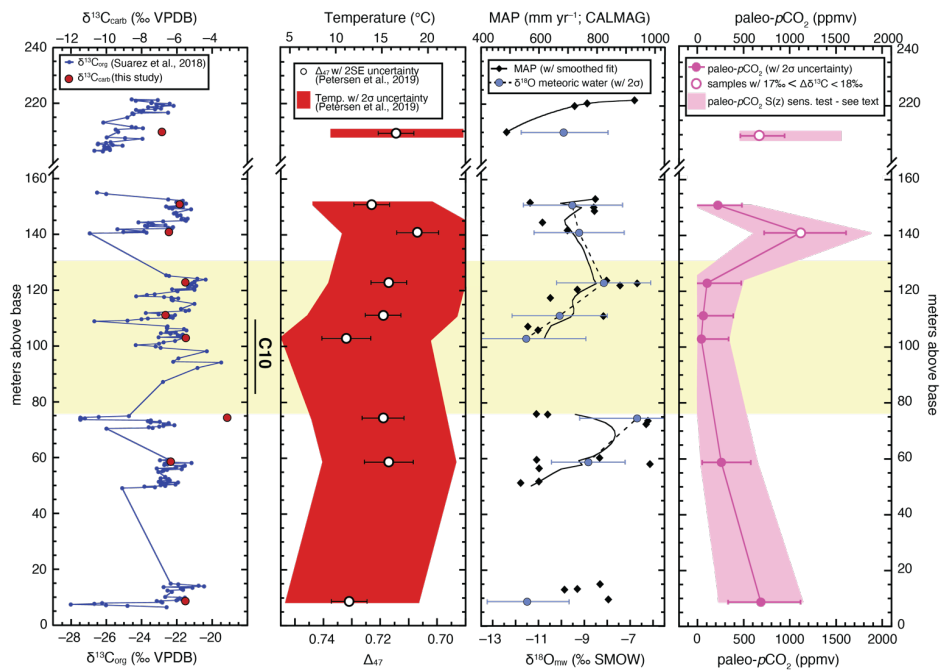
Figure 5. Multiproxy climate records and record interpretations from the White Pagoda Site, including $\delta^{13}C_{org}$ **of Suarez et al. (2018) and our new records of carbonate** $\delta^{13}C$, Δ_{47} **(with 2SE uncertainty), and temperature (with** 2σ **uncertainty), MAP and** $\delta^{18}O_{mw}$ **(with** 2σ **uncertainty), and atmospheric paleo-**p**CO_2 with** 2σ **and additional S(z) sensitivity test (see main text; non-positive calculated values are not displayed). The C10 interval has been highlighted. Note the break in depth scale at ~165 meters.**
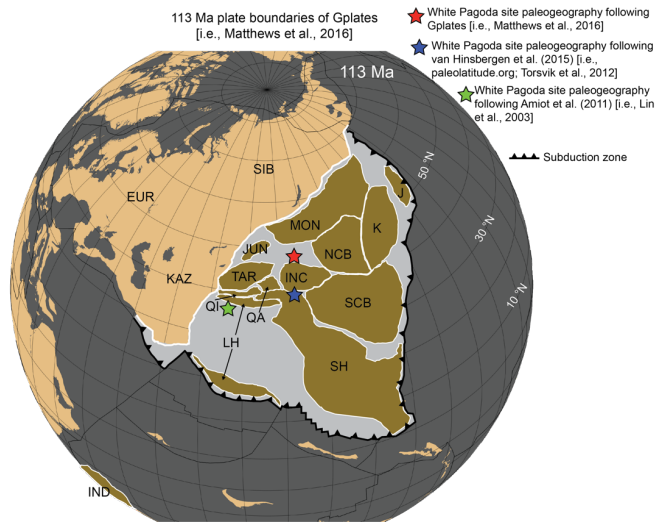
840

Figure 6. Paleogeographic reconstruction of plate boundaries ca. 113 Ma (Matthews et al., 2016) using Gplates software. Approximate location of the White Pagoda site following Matthews et al. (2016) is plotted in red. Additional paleogeographic reconstructions are also plotted for comparison (Lin et al., 2003; Torsvik et al., 2012), though these paleolocations are inconsistent with plate boundary reconstructions shown here (i.e., do not follow Matthews et al. (2016)). The Aptian-Albian paleolatitude using Gplates software is more consistent with the cooler temperatures indicated by clumped isotope paleothermometry.

845

Deleted: shift in

Deleted:
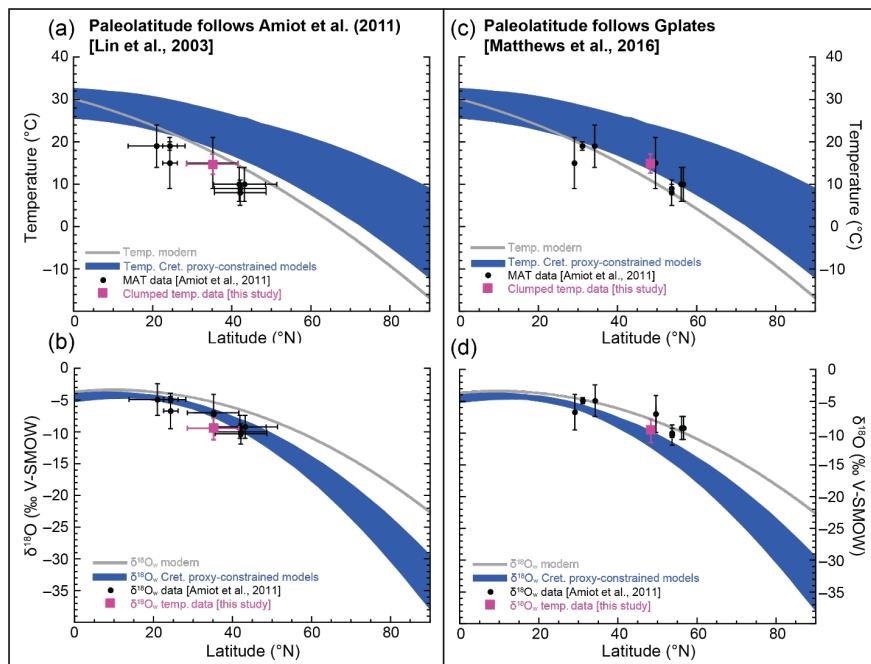
Figure 7. Northern hemisphere latitudinal gradients of temperature and meteoric water δ¹⁸O for the mid-Cretaceous (Barremian-Albian). Our mean record data (pink) and the data of Amiot et al. (2011) (black) are plotted with a range in modeled gradients of Cretaceous climate as a function of latitude (blue shaded area) compiled in Suarez et al. (2011a). Details on models included in this range are in main text. Modern temperature and meteoric water δ¹⁸O (grey lines) are plotted following Rozanski et al. (1993). 1σ uncertainty is included for all data. Two paleolatitude reconstructions are considered: Lin et al. (2003) (panels a and b) and Matthews et al. (2016) (panels c and d). Uncertainty in latitude is included in panels a and b; reconstructions of Matthews et al. (2016) do not provide uncertainty.

Table 1. Primary carbonate stable isotope data measured at KU ($\delta^{13}C$ and $\delta^{18}O$) for White Pagoda Site. $\Delta\delta^{13}C$ calculated with $\delta^{13}C_{org}$ of Suarez et al. (2018).

Sample	Composite section (meters above base)	microfacies	n	$\delta^{13}C$ mean (‰ VPDB)	$\delta^{18}O$ mean (‰ VPDB)	$\delta^{13}C$ 2σ (‰ VPDB)	$\delta^{18}O$ 2σ (‰ VPDB)	$\delta^{13}C_{org}$ (‰ VPDB)	$\Delta\delta^{13}C$ ($\delta^{13}C_{carb}$- $\delta^{13}C_{org}$) (‰ VPDB)
3-021	8.75	(i)	6	−6.26	−10.89	0.32	0.36	−23.14	16.65
3A-097	58.75	(i)	9	−7.02	−9.16	0.64	0.16	−22.55	15.53
3B-021	74.50	(ii)	8	−3.86	−6.69	0.12	0.09	−27.48	23.62
3E-001	103.00	(ii)	7	−6.45	−11.12	0.24	0.43	−21.59	14.99
3F-019	111.25	mix of (i) & (ii)	9	−7.45	−10.19	0.21	0.37	−22.11	14.66
3H-014	123.00	(i)	7	−6.33	−8.43	0.31	0.43	−21.00	14.67
6-003	141.00	(ii)	9	−7.07	−10.35	0.63	0.55	−25.04	17.97
6-042	150.90	(ii)	11	−6.36	−9.46	0.54	0.54	−21.97	15.61
4-038	209.85	(i)	6	−7.61	−10.21	0.17	0.23	−25.33	17.72

Table 2. Primary carbonate stable isotope data measured at CU Boulder (Δ_{47}, $\delta^{13}C$ and $\delta^{18}O$) for White Pagoda Site. Clumped isotopes and interpreted temperatures follow Petersen et al. (2019). Meteoric water $\delta^{18}O$ calculated from $\delta^{18}O_{carb}$ (CU Boulder measured) and clumped temperatures following Friedman and O'Neil (1977).

Sample	Composite section (meters above base)	n	$\delta^{13}C$ mean (‰ VPDB)	$\delta^{18}O$ mean (‰ VPDB)	$\delta^{13}C$ 2σ (‰ VPDB)	$\delta^{18}O$ 2σ (‰ VPDB)	Δ_{47} mean (‰)	Δ_{47} 2SE (‰)	T (°C)	T 2σ (°C)	$\delta^{18}O_{water}$ (‰ SMOW)	$\delta^{18}O_{water}$ 2σ (‰ SMOW)
3-021	8.75	4	−5.95	−10.99	0.16	0.33	0.731	0.006	11.4	+7.5/−7.0	−11.5	1.90
3A-097	58.75	3	−6.76	−9.30	0.05	0.34	0.717	0.008	15.9	+7.5/−7.0	−8.8	1.90
3B-021	74.50	4	−3.67	−6.98	0.08	0.80	0.719	0.007	15.0	+8.8/−8.1	−6.7	2.60
3E-001	103.00	4	−5.98	−10.98	0.23	0.68	0.732	0.008	11.1	+9.8/−8.9	−11.5	2.80
3F-019	111.25	4	−7.05	−10.38	0.14	0.62	0.719	0.006	15.1	+7.8/−7.2	−10.1	2.30
3H-014	123.00	4	−5.95	−8.63	0.16	0.35	0.717	0.006	15.9	+7.9/−7.3	−8.2	2.00
6-003	141.00	4	−6.86	−10.32	0.03	0.27	0.707	0.007	18.8	+9.2/−8.4	−9.2	2.10
6-042	150.90	4	−6.27	−9.60	0.04	0.61	0.723	0.006	14.0	+7.7/−7.1	−9.5	2.20
4-038	209.85	4	−7.24	−10.32	0.08	0.26	0.715	0.006	16.5	+7.9/−7.3	−9.7	1.90

Table 3. Lithologic and CALMAG (see text for details) data, with interpreted mean annual precipitation (MAP) for White Pagoda Site samples. All samples listed here are derived from interpreted B horizons of paleosols.

Sample	Composite section (meters above base)	Lithology	CALMAG	MAP (mm/yr; CALMAG)
3-021	8.75	mudstone	55.4	822
3-035	12.25	mudstone	47.9	651
3-036	12.50	fine sandstone	50.1	701
3-043	14.25	mudstone	54.0	790
3A-069	50.50	mudstone	40.4	481
3A-071	51.00	mudstone	43.5	552
3A-085	55.75	mudstone	43.6	553
3A-091	57.25	mudstone	62.6	984
3A-097	58.75	mudstone	43.1	543
3A-100	59.50	mudstone	54.0	788
3B-009	71.50	mudstone	61.9	969
3B-014	72.75	mudstone	62.2	976
3B-023	75.00	mudstone	45.0	586
3B-024	75.25	mudstone	43.1	542
3E-010	105.25	mudstone	43.3	548
3F-001	106.50	mudstone	41.7	509
3F-015	110.25	mudstone	54.6	803
3G-003	116.75	mudstone	45.5	596
3H-001	119.75	mudstone	50.1	701
3H-007	121.25	mudstone	57.4	867
3H-010	122.00	mudstone	60.4	934
3H-014	123.00	claystone	55.1	815
6-003	141.00	silty mudstone	48.4	663
6-014	143.75	sandy siltstone	44.1	566
6-030	147.90	mudstone	53.0	768
6-035	149.15	mudstone	52.9	765
6-042	150.90	carb. mudstone	42.0	517
6-047	152.15	carb. mudstone	53.2	771
4-042	210.85	mudstone	40.2	476
4-077	219.95	mudstone	49.9	697
4-081	220.95	muddy sandstone	51.7	738
4-085	221.95	muddy sandstone	58.5	892

Table 4. Atmospheric pCO_2 calculated using $\delta^{13}C_s$ (from $\delta^{13}C_{carb}$ with temperature-dependent enrichment factor; Romanek et al., 1992; 2σ uncertainty in $\delta^{13}C_{carb}$ and temperature propagated), $\delta^{13}C_a$ (average Atlantic bulk carbonate for C isotope segments following Bralower et al. (1999) with DIC-atmosphere fractionation of −8.23‰), $\delta^{13}C_r$ (organic C record of Suarez et al. (2018) with 2σ analytical uncertainty [0.26‰] propagated), and S(z) (estimated from MAP following Cotton and Sheldon (2012)). pCO_2 +* and pCO_2 –* indicate S(z) sensitivity test with same 2σ uncertainty and large S(z) range (see text for details). All $\delta^{13}C$ values reported are relative to VPDB.

Sample	Composite section (meters above base)	C isotope segment	$\delta^{13}C_s$ (‰)	$\delta^{13}C_a$ (‰)	$\delta^{13}C_r$ (‰)	S(z) (MAP-derived)	pCO_2 (ppmv)	pCO_2 + (ppmv)	pCO_2 – (ppmv)	pCO_2 +* (ppmv)	pCO_2 –* (ppmv)
3-021	8.75	C6	−16.87	−4.28	−23.14	4393	686	423	354	447	469
3A-097	58.75	C8	−17.09	−4.38	−22.55	2810	257	291	248	370	250
3E-001	103.00	C10	−17.09	−4.18	−21.59	2835	42	299	233	301	233
3F-019	111.25	C10	−17.62	−4.28	−22.11	4281	62	345	285	346	286
3H-014	123.00	C11	−16.40	−4.18	−21.00	4353	103	403	331	404	334
6-003	141.00	C12	−16.79	−4.43	−25.04	3488	1116	519	418	780	539
6-042	150.90	C12	−16.66	−4.38	−21.97	2661	218	275	230	350	231
4-038	209.85	C15	−17.61	−5.38	−25.33	2427	682	270	219	853	219